

# Dark magnetohydrodynamics: Black hole accretion in superradiant dark photon clouds

Shuo Xin<sup>1,2</sup> and Elias R. Most<sup>3,4</sup>

<sup>1</sup>*SLAC National Accelerator Laboratory, Stanford University, Stanford, CA 94309, USA*

<sup>2</sup>*Physics Department, Stanford University, Stanford, CA 94305, USA*

<sup>3</sup>*TAPIR, Mailcode 350-17, California Institute of Technology, Pasadena, CA 91125, USA*

<sup>4</sup>*Walter Burke Institute for Theoretical Physics, California Institute of Technology, Pasadena, CA 91125, USA*

Black holes threaded by massive vector fields can be subject to a superradiant instability, growing a cloud of massive vector particles around it. In this work, we consider what happens if such a dark matter candidate field mimicking a dark photon interacts with an accretion flow onto the black hole. By including a kinetic mixing term with the standard model photon, we extend the commonly used equations of general-relativistic magnetohydrodynamics to a dark photon constituent. The coupling to the dark photon then appears as an effective dynamo term together with a dark Lorentz force acting on the accreting matter. We numerically study the interactions between the superradiant dark photon cloud and the inner accretion flow by solving the coupled system in full numerical relativity. By parameterically varying the mixing parameter between dark and standard model sector, we provide a first investigation of how the accretion flow could be modified. Depending on the coupling strength, our solutions exhibit increased wind launching, as well as oscillation modes in the disk.

## I. INTRODUCTION

The study of physics near strong gravity sources has drawn increasing attention. Gravitational wave detections of merging stellar mass compact objects have provided new insights into the theory of relativity [1–8]. With upcoming space-based detectors [9], as well as potential constraints on the emission geometry of black holes [10–12], we have excellent opportunities to test extensions of general relativity [13–15]. Apart from modified gravity, black holes (BH) also have the potential to probe new states of (dark) matter [16, 17]. Many different dark matter candidates have been brought forward including ultralight vector bosons [18–20], axions [21, 22], scalar fields [23] to just name a few. Understanding whether and how they could modify the dynamics of gravitational wave emission and matter flows (environmental effects) around black holes is one of the key challenges for the LISA mission [24, 25].

One particular class of models are ultralight massive bosons, e.g. the QCD axion [21, 22, 26] and dark photon [27–30]. Adding to their appeal in this context, massive boson fields threading black holes can result in superradiance [22, 31]. For sufficiently high black hole spin, bosonic particles subject to superradiance will undergo exponential growth outside the angular momentum barrier of Kerr black holes, extracting rotational energy from the hole, and form a macroscopic bound state. In other words, black holes may self-produce copious amounts of dark matter through general-relativistic instabilities, making them an ideal playground to investigate this kind of dark matter models. Over the past years, a large body of literature has been devoted toward understanding this phenomenon and its implications analytically (e.g., [32–38]) and through numerical simulations (e.g., [39–43]).

At the same time, analytic computations of massive vector mode spectra have matured considerably. Early calculations have provided approximate characteristic frequencies and growth/decay rates [44–51]. Recent work by Frolov, Kr-tous, Kubiznak and Santos (FKKS) on the separability of the

Teukolsky-like perturbation equation [36] has enabled subsequent analytic calculations of quasi-normal modes to higher accuracy [37, 38], including potential gravitational wave signatures [40, 42], see also Refs. [17, 52–55] for proposed search strategies.

In addition to gravitational wave emission, a superradiant dark photon cloud may also leave imprints through a potential coupling to the standard model. In many astrophysical environments, black holes are surrounded by gaseous accretion flows, powering strong outflows and electromagnetic emission [56–59]. Depending on the coupling strength, it is conceivable that interactions with the dark photon cloud through kinetic mixing terms in the Lagrangian could modify astrophysical observables. Recent work by Siemonsen et al. [60] has studied the dynamics of a force-free pair plasma modulated by interactions with such a dark photon cloud around an isolated stellar mass black hole formed in a merger, finding potential X-ray signatures of dark matter interactions.

While force-free plasmas are applicable in the absence of external gas, merging black holes in disk around active galactic nuclei (AGN), or even the AGN itself will lead to the presence of matter and external magnetic field. In this environment, rather than relying on magnetic field dynamics entirely sourced by the dark photon cloud, the accretion flow will likely be governed by the gas, with potential modifications through the dark matter cloud. In the present work, we target precisely such an environment.

Due to the highly non-linear interplay of dynamical strong gravity, (dark) matter and electromagnetic dynamics, a full investigation can only be carried out numerically. While accretion flows onto black hole mimickers have been investigated extensively [61–63], works in dynamical gravity have so far largely been limited to scalar field dynamics (see [60] for magnetospheric dynamics only).

In this paper we numerically study accretion flows through (self-gravitating) superradiant dark photon clouds in the dynamical spacetime of a black hole. To this end, we derive a new set of evolution equations that couple commonly used general-relativistic magnetohydrodynamics (GRMHD) equations [64] with those of a Proca field [40]. We provide a first

assessment of the resulting accretion flow structure and discuss potential implications of the coupling between dark and standard model sector.

This paper is structured as follows. We briefly introduce the physics of superradiance and GRMHD in Sec. II and explain our formulation and numerical implementation in Sec. III. Examples of black hole magnetospheric dynamics and accretion disks are shown in Sec. IV and we conclude in Sec. V. Throughout this paper, we use geometrized units ( $G = c = 1$ ) and measure quantities by respective powers of the black hole mass  $M$ . We adopt a four-dimensional metric  $g_{\mu\nu}$  with signature  $(-, +, +, +)$ .

## II. PHYSICAL PICTURE

Superradiance is a prominent feature of massive bosonic fields around spinning black holes. In black hole perturbation theory it is a family of exponentially growing solutions of quasi-normal modes (QNM). We here consider Newman-Penrose (NP) scalars  $\psi$  constructed from fields of spin weight  $S$ , or vector fields from  $A_\mu = B_{\mu\nu}\nabla^\nu\psi$  with polarisation tensor  $B_{\mu\nu}$  of weight  $S$  [36–38], in a Kerr black hole background with spin parameter  $a$ . Separating the field into spherical,  $S(\theta)e^{im\phi}$  and radial,  $R(r)$ , parts

$$\psi = e^{-i\omega t + m\phi} R(r) S(\theta), \quad (1)$$

radial perturbations are governed by Teukolsky-like equations of the form [65–67]

$$\Delta^2 \frac{d}{dr} \left( \frac{1}{\Delta} \frac{dR}{dr} \right) - V(r)R = 0, \quad (2)$$

where  $\Delta = r^2 - 2Mr + a^2$ . Here  $\omega$  is the effective mode frequency of the oscillation. For massless fields such as electromagnetic fields and gravitational perturbations,  $V(r)$  acts as an angular momentum barrier, which is only nontrivial around the black hole ergosphere, allowing simple sinusoidal wave solutions near the horizon  $r_+ = M + \sqrt{M^2 - a^2}$  and infinity (after proper transformations such as Sasaki-Nakamura [68–71]). One prominent feature of this angular momentum barrier is that the energy reflectivity is larger than 1 when the frequency of the field perturbation is lower than the angular frequency of the outer horizon  $\Omega_+ = a/(r_+^2 + a^2)$ . Heuristically this is dual to the Penrose process of point particles, allowing the possibility of extracting rotational energy from the black hole.

In analogy with bound orbits, if an additional outer barrier exists in the potential  $V(r)$ , we have the possibility of forming bound states of dark matter perturbations around the black hole. Near horizon features can modify  $V(r)$  inside, and depending on the reflectivity of the barrier near the horizon, this may lead to a superradiant ergoregion instability (large reflectivity) [72–74] or wave echoes (small reflectivity) [75–79]. We may also alter the potential from the outside. When the associated dark particle is of mass  $m_\gamma = \hbar\mu$ , additional features at large radii near  $r \sim 1/m_\gamma$  could naturally arise [22]. Such ultralight massive bosons are also promising candidates for

dark matter [80]. Naively, we may expect particles propagating with real frequencies  $\omega_R \sim \mu$  to form a bound state and exponentially grow due to superradiance at a rate  $\omega_I \propto (\Omega_+ - \mu)$ , ultimately stabilizing at “floating” orbits [81].

Perturbative calculations show that for the QNM of massive vector fields characterized by overtone number  $n$ , azimuthal “magnetic” number  $m$  and polarisation number  $S$  (there are different definitions in literature, we adopt the notation in works after FKKS [36–38]), the frequency spectra, to leading order of  $\mu$ , is given by [32–38, 50]

$$\omega_R \approx \mu \left( 1 - \frac{(M\mu)^2}{2(|m| + n + S + 1)^2} \right), \quad (3)$$

and growth rate

$$\omega_I \approx (m\Omega_+ - \omega_R) (M\mu)^{4|m|+5+2S}. \quad (4)$$

Strong superradiance is expected for (near) extremal spin, earlier numerical simulations has also shown an  $M\omega_I \approx 10^{-4}$  for  $a = 0.99$  black hole [82]. Also the rate is highly dependent on the dark “fine-structure” constant [60, 83]  $\alpha' = M\mu$ . The growth is most effective when the black hole mass  $M$  and the dark photon mass  $\mu$  satisfy

$$\alpha' = 1.336 \left( \frac{M}{10^6 M_\odot} \right) \left( \frac{10^{-16} \text{eV}}{m_\gamma} \right) \sim 0.1. \quad (5)$$

After the superradiant growth, a stable “cloud” of dark photon is formed around the black hole, mainly occupying the  $n = 0, m = 1, S = -1$  state. Oscillation of the field emit gravitational waves, making the field decay with a power law over time,  $t$ , [45, 84]

$$\psi \sim t^{-p}. \quad (6)$$

It can be shown that initially when the cloud grows  $p = |m| + s + \frac{3}{2}$ , which transitions to  $p = -5/6$  in the saturated state [45, 84]. This is also approximately observed in early numerical simulations [39, 40]. Recent studies, especially after the separation of variables worked out by FKKS [36], also show growing interest in higher overtones, higher multiples, and subdominant polarisations. These subdominant modes can occupy different spatial locations. Polarisations  $S = 0, +1$  are peaked further away from the black hole while the dominant modes with  $S = -1$  are confined near the horizon. They also lead to beating features in gravitational wave emission [37, 38].

Such macroscopic dark photon clouds can introduce rich physical effects by coupling to the visible sector. Even if the electromagnetic environment around the black hole is vacuum, the dark photon could potentially create turbulent dynamics in the standard model matter, leading to dissipation and emission [60].

In low energy effective theories that are renormalizable, the relevant interaction is kinetic mixing through a term  $\epsilon\mu^2 A'_\mu A^\mu$  where  $A_\mu$  is the vector potential of visible electromagnetic fields and  $A'_\mu$  of dark photon fields. As will be detailed in Sec. III, this leads to terms proportional to  $\epsilon\alpha'^2 A'^\mu$  in the effective

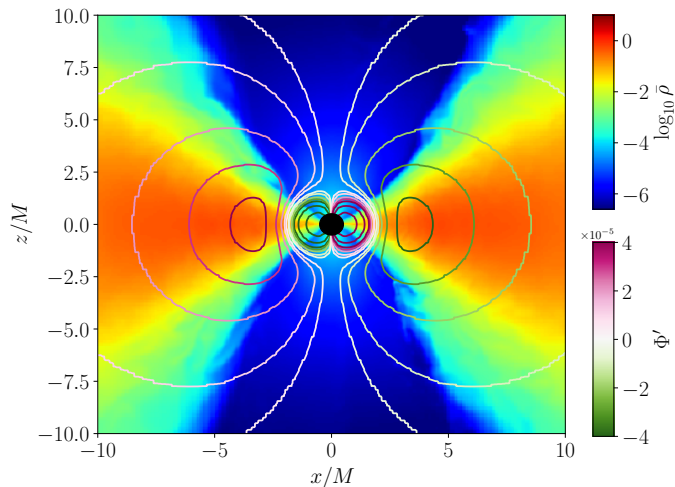


FIG. 1. Schematic illustration of the overlap between the accretion disk and the dark photon cloud around a black hole (center). Shown in color are the rest-mass density,  $\bar{\rho}$ , of the accretion disk and contours of the Proca charge  $\Phi' = A'_\mu r^\mu$  in the dark photon cloud. Shown is an initial accretion snapshot in quasi-steady state after  $t = 2000M$ , shortly before turning on the coupling of the dark photon field to the accretion flow, where  $M$  is the black hole mass.

Maxwell equations, normalized by black hole mass  $M$ . Therefore the role of the superradiant cloud depends on the relative scale of the dark  $A'_\mu$  and the visible  $A_\mu$  sectors.

The strength of the Proca fields is determined by the total energy endowed to the cloud during the superradiant growth. This process has been intensively explored both by numerical simulations [39–42] and perturbative calculations [38, 60]. This leads to a spin down of the black hole from initial spins  $a_i$  to final spins  $a_f$ , with rotational energy mainly extracted by dark photon cloud. An estimate for the magnitude of the total cloud mass  $M'$  is [60]

$$\frac{M'}{M} \sim \alpha' (a_i - a_f). \quad (7)$$

The radial distribution of this cloud is mainly confined inside a radius of  $r_0 \approx M/\alpha'^2$ , as shown for the case of  $\alpha' = 0.4$  in Fig. 2. Inside this radius the magnitude of dark electromagnetic field is estimated by [60]

$$E' \sim (M')^{1/2} r_0^{-3/2}, \quad B' \sim (M')^{1/2} r_0^{-5/2} \mu^{-1}. \quad (8)$$

When coupled to the visible sector, this may introduce a modification of the accretion flow structure near the black hole. As an order of magnitude estimate, for a strong “fine-structure” constant  $\alpha' \sim 0.1$ , the strength of this dark source corresponds to a scale of visible magnetic fields of

$$B \sim 2.4 \left( \frac{M'}{10^{-2}M} \right)^{1/2} \left( \frac{\alpha'}{0.1} \right)^4 \left( \frac{\epsilon}{10^{-8}} \right) \left( \frac{10^6 M_\odot}{M} \right) \text{G}, \quad (9)$$

which is typical for magnetospheres and jet regions near supermassive black holes in the parameter ranges we explore [85]. Also note that in mass units, such magnetic fields are

of order  $\sim 10^{-10} M^{-1}$  and the backreaction of it on the spacetime can be ignored, i.e. the magnetosphere and accretion disk are not self-gravitating, while the dark sector is macroscopic, comparable to black hole mass in extreme cases.

In simulations presented in this work, we explore parameters in ranges that are both astrophysically common and allow for effective superradiance. The magnetic fields near black holes are of order up to  $10^2$  Gauss and electron density in the plasma is of order  $10^{10} \text{cm}^{-3}$ . The black hole spin is set to  $a = 0.9M$  [86]. To allow for a significant amount of dark photons we mostly explored the  $\alpha' = 0.4$  case when coupled to the visible sector. The kinetic mixing (coupling) constant  $\epsilon$  is of order  $10^{-9}$  to  $10^{-7}$ . The black hole mass only appears as an overall scale, and is understood to be between  $10^6$  to  $10^9$  solar mass to allow for reasonable physical interpretation. Therefore, the dark photon mass range we explore will be between  $10^{-19} eV < m_\gamma < 10^{-16} eV$ .

The energy and angular momentum of the superradiant dark photon cloud in the base state mainly resides in a toroidal region around the black hole, as shown both by perturbation theory calculations and numerical simulations [38, 40–42, 60]. This will allow for interesting interplay of it with accretion disks that astrophysical black holes often endow, as schematically illustrated in Fig. 1. In our studies, we see large scale oscillation modes excited by the Proca field inside the disk and the launching of disk wind by mechanism beyond the traditional Blandford-Payne process due to the “dark” Lorentz force that we introduce in the next section.

### III. METHODS

#### A. Dark magnetohydrodynamics in dynamical spacetimes

Accretion disks are commonly observed around astrophysical black holes [87]. The relativistic dynamics of the plasma and magnetic field in the strong gravity background is the central engine that powers accretion, wind, and jets [56–59, 88–91]. Accurate (GR-)MHD simulations are required for describing such astrophysical settings. For our purpose, in addition, we also need to include the system of equations for a massive Proca field, representing the dark photon. Due to the superradiant nature of massive bosonic fields around spinning black holes, the strength of the Proca field is macroscopic. The back-reaction of them on the spacetime can, therefore, not be ignored. In the following, we outline our approach towards the combined modeling of these effects.

The action that couples the electromagnetic vector potential  $A^\mu$  and Proca field  $X^\mu$  (in mass basis) with gravity is [40, 60, 92]

$$\mathcal{S} = \int d^4x \sqrt{-g} \left( \frac{R}{4} - \frac{1}{4} W_{\mu\nu} W^{\mu\nu} - \frac{1}{4} F_{\mu\nu} F^{\mu\nu} - \frac{\mu^2}{2} X_\mu X^\mu + \frac{\epsilon}{2} F_{\mu\nu} W^{\mu\nu} + \mathcal{J}_\mu A^\mu \right), \quad (10)$$

where we have defined the field strength tensors  $F_{\mu\nu} = \nabla_{[\mu} A_{\nu]}$ ,  $W_{\mu\nu} = \nabla_{[\mu} X_{\nu]}$ . Here,  $R$  is the Ricci scalar and  $\mathcal{J}^\mu$  the

electric current. The coupling between the dark and visible sectors is expressed in terms of a small coupling parameter  $\epsilon$  [93]. Going to the interaction basis  $A'_\mu$  with  $X_\mu = A'_\mu + \epsilon A_\mu$ ,  $W_{\mu\nu} = F'_{\mu\nu} + \epsilon F_{\mu\nu}$  where  $F'_{\mu\nu} = \nabla_{[\mu} A'_{\nu]}$ :

$$\mathcal{S} = \int d^4x \sqrt{-g} \left( \frac{R}{4} - \frac{1}{4} F'_{\mu\nu} F'^{\mu\nu} - \frac{1}{4} F_{\mu\nu} F^{\mu\nu} - \frac{\mu^2}{2} A'_\mu A'^\mu - \epsilon \mu^2 A'_\mu A^\mu + \mathcal{J}_\mu A^\mu \right). \quad (11)$$

The equations of motion for the Proca field  $A'_\mu$  and the ordinary electromagnetic field then follow as,

$$\nabla_\nu F'^{\mu\nu} = -\mu^2 A'^\mu + \epsilon \mu^2 A^\mu, \quad (12)$$

$$\nabla_\nu F^{\mu\nu} = \mathcal{J}^\mu - \epsilon \mu^2 A'^\mu. \quad (13)$$

As we see above, the dark photon effectively contributes as an additional current  $-\epsilon \mu^2 A'^\mu$  to the Maxwell equations. The presence of this current has important consequences. As we can see in the absence of a coupling,  $\epsilon = 0$ , it immediately implies that the dark photon field needs to be in Lorenz gauge,  $\nabla_\mu A'^\mu = 0$ , which in the presence of a coupling to the visible sector implies that the vector potential  $A^\mu$  needs to be in the same gauge,  $\nabla_\mu A^\mu = 0$ . Since  $A'^\mu$  also describes the current, it further implies that the gauge scalar  $\Phi' \simeq A'^0$  at the same time describes a dark charge. It will therefore be convenient to visualize the dark photon field this way.

The main challenge is now to couple the dark and visible sectors in a way compatible with the usual ideal MHD assumption, that the resistivity  $\eta$  of the plasma vanishes, screening any electric field  $e^\mu = u_\nu F^{\mu\nu}$  in the fluid frame given by the plasma four-velocity  $u^\mu$ . On a practical level, retaining the dark photon interaction current, will naturally violate this assumption. However, following a similar approach recently employed for the feedback of mean-field dynamo terms [94], we can perturbatively include the current in the induction equation to leading order, i.e.,  $e^\mu \simeq \mathcal{O}(\epsilon)$ , without changing the main character of the evolution system. Such a coupling is naturally appropriate if the impact of the dark photon on the plasma is small, or more precisely if the coupling timescale is much longer than the resistive timescale of the plasma.

Following [94], we formulate the total Ohm's law of the system by borrowing from relativistic two-fluid plasmas [95],

$$\tau u^\nu \nabla_\nu \mathcal{J}^\mu = -\mathcal{J}^\mu - \epsilon \mu^2 A'^\mu + \eta^{-1} e^\mu, \quad (14)$$

where  $\tau$  is the effective collisional timescale of the plasma. The ideal MHD limit is obtained by assuming effective collisionality and resistivity  $\tau, \eta \rightarrow 0$ . In practice, in our simulations  $\eta$  will be non-zero effectively due to numerical resistivity from the discretization of the equations. In this spirit, we now approach the perfectly conducting limit, such that  $\tau = 0$ , but the feedback of the dark sector will be retained relative to the grid resistivity, i.e.,

$$e^\mu \approx \frac{\epsilon}{\sigma} \mu^2 A'^\mu, \quad (15)$$

We use coupling constant rescaled by conductivity  $\bar{\epsilon} = \epsilon/\sigma$  to quantify this effect.

The equation of motion for the spacetime metric is the usual Einstein's equation

$$R_{\mu\nu} - \frac{1}{2} R g_{\mu\nu} = 8\pi T_{\mu\nu}^{\text{total}}, \quad (16)$$

where  $R_{\mu\nu}$  is the Ricci tensor and  $T_{\mu\nu}^{\text{total}}$  the total energy-momentum tensor. The total energy momentum tensor contains contributions from the electromagnetic fields, Proca field and the fluid. The specification of  $T_{\mu\nu}^{\text{total}}$  in terms of fluid density, pressure and velocity defines the property of the plasma we are considering.

We describe an accreting plasma around black holes as an ideal fluid with rest-mass density  $\rho$  and 4-velocity  $u_\mu$ . The equations of motion for the fluid are given by continuity  $\nabla_\mu(\rho u^\mu) = 0$  and conservation of total energy-momentum  $\nabla_\nu T_{\text{total}}^{\mu\nu} = 0$  [96], where the total energy-momentum gets contribution from the electromagnetic field, Proca field and ideal fluid:

$$T_{\mu\nu}^{\text{total}} = T_{\mu\nu}^{\text{EM+fluid}} + T_{\mu\nu}^{\text{Proca}}, \quad (17)$$

$$T_{\mu\nu}^{\text{EM+fluid}} = F_{\mu\rho} F_\nu^\rho - \frac{1}{4} g_{\mu\nu} F^{\alpha\beta} F_{\alpha\beta} + \rho h u^\mu u^\nu + p g^{\mu\nu}, \quad (18)$$

$$T_{\mu\nu}^{\text{Proca}} = F'_{\mu\rho} F'^\rho_\nu - \frac{1}{4} g_{\mu\nu} F'^{\alpha\beta} F'_{\alpha\beta} + \mu^2 \left( A'_\mu A'_\nu - \frac{1}{2} g_{\mu\nu} A'^\alpha A'_\alpha \right), \quad (19)$$

where  $p$  is pressure and  $h$  is the specific enthalpy. We have also included the electromagnetic contribution in a combined tensor  $T_{\mu\nu}^{\text{EM+fluid}}$ .

## B. 3+1 decomposition

In this work we adopt the 3+1 decomposition of the spacetime metric,  $g_{\mu\nu}$ , [97]

$$ds^2 = (-\alpha^2 + \beta_i \beta^i) dt^2 + 2\beta_i dx^i dt + \gamma_{ij} dx^i dx^j, \quad (20)$$

where  $\alpha$  is the lapse function,  $\beta^i$  the shift, and  $\gamma_{ij}$  the induced metric on the hypersurface normal to  $n_\mu = (-\alpha, 0, 0, 0)$ . The metric dynamics in the 3+1 decomposition is governed by the ADM equations [64, 96] with total energy-momentum tensor given above:

$$\begin{aligned} \partial_t \gamma_{ij} &= -2\alpha K_{ij} + \mathcal{L}_\beta \gamma_{ij} \\ \partial_t K_{ij} &= -D_i D_j \alpha + \alpha (R_{ij} - 2K_{ik} K_j^k + K K_{ij}) \\ &\quad + \mathcal{L}_\beta K_{ij} - 8\pi \alpha \left( S_{ij}^{\text{total}} - \frac{1}{2} \gamma_{ij} (S^{\text{total}} - \rho) \right) \end{aligned} \quad (21)$$

where  $D_i$  is covariant derivative with respect to spatial metric  $\gamma_{ij}$ ,  $\mathcal{L}$  denotes Lie derivative,  $K_{ij}$  is extrinsic curvature and the evolution equation of spatial metric is the definition of  $K_{ij}$ .  $S^{\text{total}} = T_{\text{total}}^{\mu\nu} n_\mu n_\nu$  and  $S_{\alpha\beta}^{\text{total}} = T_{\mu\nu}^{\text{total}} \gamma_\alpha^\mu \gamma_\beta^\nu$  are normal and spatial



projections of total energy-momentum tensor. We solve the ADM equations using the augmented Z4c system [98, 99].

We can further simplify the expression for the energy momentum tensor. Combining the relation between the normal and comoving electric field

$$E^\mu = n_\nu F^{\mu\nu} = -\varepsilon^{\mu\nu\alpha} v_\nu B_\alpha + \Gamma^{-1}(e^\mu + n^\mu e^\nu n_\nu), \quad (22)$$

with the expression for the dark matter induced non-ideal electric field (15), we find

$$E^\mu = -\varepsilon^{\mu\nu\alpha} v_\nu B_\alpha + \bar{\varepsilon}\mu^2 \Gamma^{-1} \mathcal{A}^\mu, \quad (23)$$

where  $\mathcal{A}^\mu = A^\mu + n^\mu A^\nu n_\nu$  is the spatial projection of Proca field. We have also introduced the Lorentz factor  $\Gamma = -n_\mu u^\mu$ . Here, the first term in Eq. (23) is the usual ideal electric field, whereas the second term represents a dark component. This is akin to an  $\alpha$ -term in the induction equation [94], albeit here the standard model magnetic field will be driven to form loops around the dark vector potential.

Using this expression for the electric field, we can now write an evolution equation (13) for the standard model magnetic vector potential in 3+1 form,

$$\partial_t \mathcal{A}_i - \varepsilon_{ijk}(\alpha v^j - \beta^j) B^k + \partial_i(\alpha \Phi - \beta^j \mathcal{A}_j) = -\alpha \bar{\varepsilon} \mu^2 \Gamma^{-1} \mathcal{A}'_i, \quad (24)$$

$$\partial_t(\sqrt{\gamma}\Phi) + \partial_j(\sqrt{\gamma}\alpha \mathcal{A}^j - \sqrt{\gamma}\beta^j \Phi) = -\alpha \kappa \sqrt{\gamma}\Phi, \quad (25)$$

where we split  $A_\mu$  into spatial component  $\mathcal{A}_i$  and time component  $\Phi = -n^\mu A_\mu$ ,  $v^i$  is the 3-velocity of fluid related to 4-velocity by  $u^\mu = \Gamma(n^\mu + v^\mu)$ . The second equation is the Lorenz gauge condition, where we have added an extra damping term parameterized by  $\kappa$  in order to maintain numerical stability [100].

We now turn to the problem of formulating evolution equation for the hydrodynamics sector. Following [64], we can express the generic energy momentum tensor of resistive GRMHD as

$$T_{\text{MHD}}^{\mu\nu} \equiv T_{\text{EM+fluid}}^{\mu\nu} = \rho h u^\mu u^\nu + \frac{1}{2}(E^2 + B^2 + 2p)g^{\mu\nu} - E^\mu E^\nu - B^\mu B^\nu + (n^\mu \varepsilon^{\nu\alpha\beta} + n^\nu \varepsilon^{\mu\alpha\beta}) E_\alpha B_\beta. \quad (26)$$

The Proca contributions lead to two modifications to ideal MHD: a) an additional nonideal current Eq. 15, b) an external source term to the energy momentum conservation law. We give a brief summary in the following paragraphs, and refer to Appendices A and B for a comprehensive discussion.

While we impose joint conservation of matter and visible EM fields, the presence of a self-gravitating dark matter cloud causes a dark Lorentz force,  $I^\mu$ , to act on the matter sector, i.e.,

$$\nabla_\nu T_{\text{MHD}}^{\mu\nu} = -\nabla_\nu T_{\text{Proca}}^{\mu\nu} = \varepsilon \mu^2 F'^{\mu\nu} A_\nu =: I^\mu. \quad (27)$$

Thus, performing the usual decomposition of the energy-momentum tensor (with subscript  $\text{MHD}$  omitted hereafter),

$S = T^{\mu\nu} n_\mu n_\nu$ ,  $S_\alpha = -T_{\mu\nu} n^\mu \gamma_\alpha^\nu$ ,  $S_{\alpha\beta} = T_{\mu\nu} \gamma_\alpha^\mu \gamma_\beta^\nu$ , we have the conserved MHD energy and momentum densities

$$S = \rho h \Gamma^2 - p + \frac{E^2 + B^2}{2}, \quad (28)$$

$$S_i = \rho h \Gamma^2 v_i + \varepsilon_{ijk} E^j B^k.$$

where the electric field  $E^i$  now includes an additional nonideal contribution from Eq. 23. This requires a revised primitive-recovery algorithm [101, 102], which we provide in Appendix B.

The modified hydrodynamic equations for the conserved quantities above in 3+1 form are (following the derivation detailed in Appendix A):

$$\partial_t(\sqrt{\gamma}\Gamma\rho) + \partial_j(\sqrt{\gamma}(\alpha v^j - \beta^j)\Gamma\rho) = 0, \quad (29)$$

$$\begin{aligned} \partial_t(\sqrt{\gamma}S) - \partial_i[\sqrt{\gamma}(\beta^i S - \alpha S^i)] \\ = \sqrt{\gamma}[\alpha K^{ij} S_{ij} - S^i D_i \alpha + \alpha \mathcal{I}_\Phi], \end{aligned} \quad (30)$$

$$\begin{aligned} \partial_t(\sqrt{\gamma}S_j) + \partial_i[\sqrt{\gamma}(\alpha S_j^i - \beta^i S_j)] \\ = \sqrt{\gamma}\left[S_i \partial_j \beta^i - S \partial_j \alpha + \frac{1}{2} S^{ik} \partial_j \gamma_{ik} + \alpha \mathcal{I}_j\right], \end{aligned} \quad (31)$$

with  $\mathcal{I}_\Phi = -n^\mu I_\mu$  and  $\mathcal{I}_\mu = I_\mu - n_\mu \mathcal{I}_\Phi$  the normal and spatial components of the energy momentum source  $I_\mu$ .

Expanding the dark electromagnetic field strength tensor  $F'_{\mu\nu} = n_\mu E'_\nu - n_\nu E'_\mu + \varepsilon_{\mu\nu\alpha} B'^\alpha$ , we have the source to MHD energy-momentum in terms of Proca  $E', B'$  fields:

$$I^\mu = \varepsilon \rho'_e (E'^\mu + \varepsilon^{\mu\alpha\beta} v_\alpha^D B'_\beta), \quad (32)$$

$$\mathcal{I}_\Phi = \varepsilon \rho'_e E'^i v_i^D, \quad (33)$$

where we have introduced the effective advection speed seen by the dark force  $(v^D)^i = A^i/\Phi$  and the effective dark charge density  $\rho'_e = \mu^2 \Phi$ . This can be understood from the interaction term  $\varepsilon \mu^2 A'_\mu A^\mu$  in the Lagrangian Eq. 11, where  $\mu^2 A^\mu$  can be interpreted as the four-current to the dark sector. For the Proca field equations we split the Proca field as  $A'_\mu = \mathcal{A}'_\mu + n_\mu \Phi'$  with normal components  $\Phi' = -n^\mu A'_\mu$ .

These additional terms in hydrodynamic equations can be intuitively understood:  $\mathcal{I}_i$  in Eq. 32 is the dark photon version of a Lorenz force, while the normal part  $\mathcal{I}_\Phi$  in Eq. 33 is ‘‘dark’’ Ohmic heating. Overall the equations are very similar to the ones outlined for the EM fields. Writing them in the form of Refs. [40, 46] but adding additional interaction with the ordinary electromagnetic field, we have

$$(\partial_t - \mathcal{L}_\beta) \mathcal{A}'_i = -\alpha E'_i - D_i(\alpha \Phi'), \quad (34)$$

$$(\partial_t - \mathcal{L}_\beta) \Phi' = \alpha K \Phi' - D_i(\alpha \mathcal{A}'_i), \quad (35)$$

$$\begin{aligned} (\partial_t - \mathcal{L}_\beta) E'^i = \varepsilon^{ijk} D_j(\alpha B'_k) + \alpha K E'^i \\ + \alpha \mu^2 \mathcal{A}'^i - \varepsilon \alpha \mu^2 \mathcal{A}^i, \end{aligned} \quad (36)$$

where the last line evolution equation for dark electric field  $E'^\mu = n_\nu F'^{\mu\nu}$ , gets additional contribution from coupling with visible sector. Here, the visible EM potential  $\mathcal{A}^i$  appears as an effective current to dark electric field.

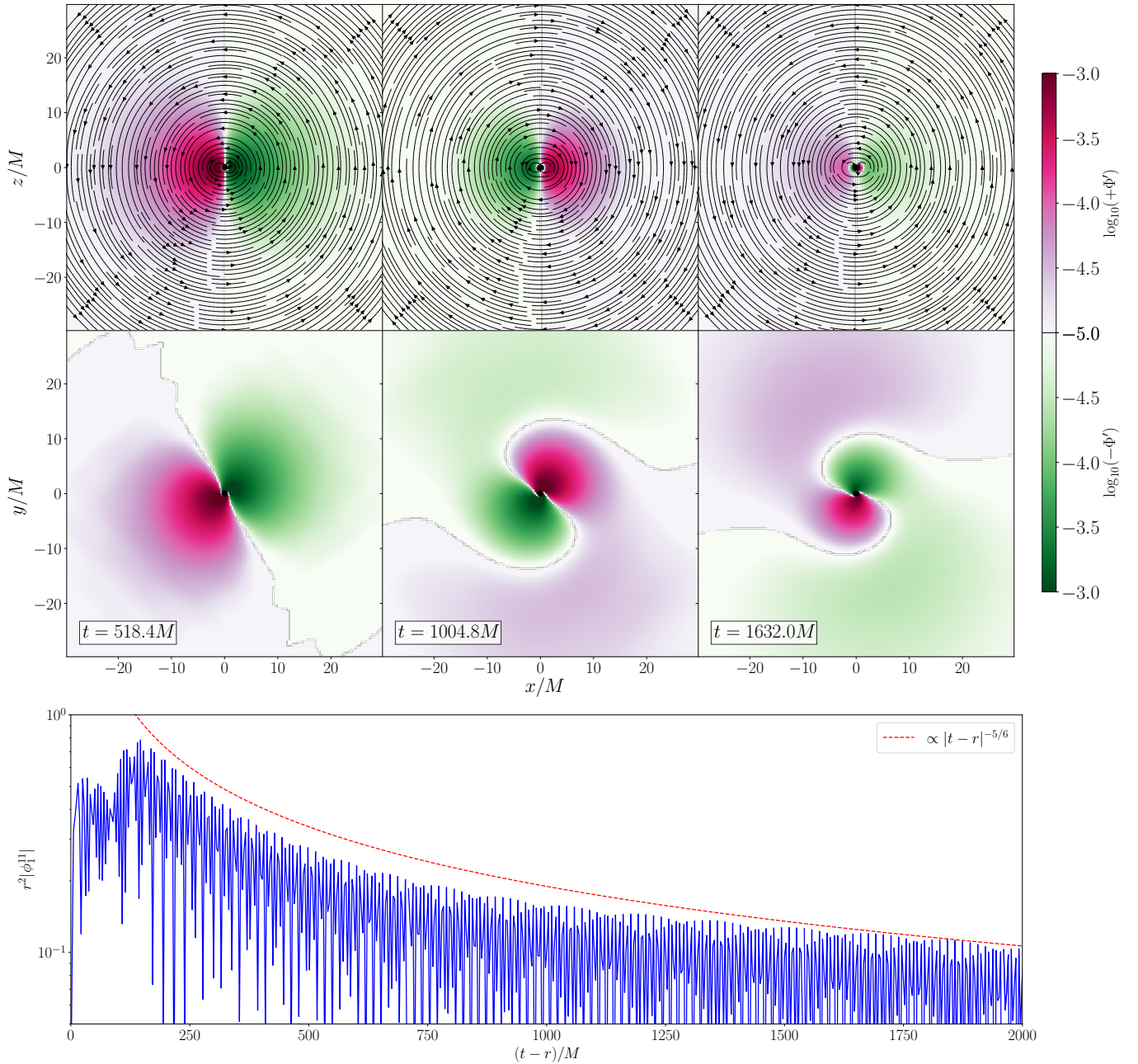


FIG. 2. Stable configuration (top) and power-law decay (bottom) of the dark photon cloud. Black solid arrows indicate the stream lines of the dark magnetic field. The strength of the Proca normal component  $\Phi'$  is color coded in blue-red, magnitudes are measured in geometric units. The blue solid curve is the time evolution of the Proca Newman-Penrose scalar  $\phi_1^{11}$  extracted at  $r = 100M$ , where  $M$  is the black hole mass. The power-law decay of the field is proportional to  $|t - r|^{-5/6}$  and is shown with a red dashed curve. The initial condition shown is set according to Eq. 37 and 38 with parameters  $\hat{C}_{11} = 0.1$ ,  $\hat{r}_0 = 6M$ ,  $\hat{\sigma} = M$ ,  $M\mu = 0.4$ .

### C. Dark photon clouds around black holes

To model a dark photon cloud around an isolated black hole, we adopt initial condition similar to the Gaussian initial condition in [40], where the normal component  $\Phi'$  follows a Gaussian radial distribution and an angular distribution of  $Y_{11}$

spherical harmonics:

$$\Phi' = \psi^{-6} \hat{C}_{11} e^{-\frac{(r-\hat{r}_0)^2}{\hat{\sigma}^2}} Y_{11}(\theta, \phi), \quad (37)$$

where  $\psi^{12} = \det\{\gamma_{ij}\}$  is the usual coefficient in conformal decomposition of spacetime evolution equations, and  $\hat{C}_{11}$ ,  $\hat{r}_0$ ,  $\hat{\sigma}$  are the strength, center and width of the Gaussian distribution. The initial dark electric field  $E'$  is set by solving a Poisson

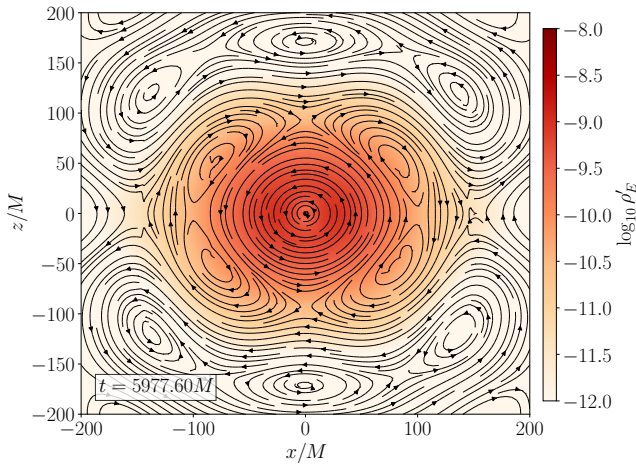


FIG. 3. Energy density  $\rho'_E = n_\mu n_\nu T^{\mu\nu}_{\text{Proca}}$  and magnetic field lines of the dark photon field. In addition to the dominant  $S = -1$  polarisation, which peaks near the black hole and decays exponentially at large radii, the radial profile of energy density exhibit a subdominant mode peaked near  $r \sim 40M$ [37]. Higher multipoles persist through late times.

equation for the dark electric field:

$$D_i E^{ri} + \mu^2 \Phi' = 0, \quad (38)$$

with the boundary condition  $E^{ri} \rightarrow 0$  at  $r \rightarrow \infty$ .

The characteristic time scale is set by the frequency of Proca field oscillation  $1/\omega_R \sim 1/\mu \sim 2.5M$ . With initial setup  $\hat{C}_{11} = 0.1$ ,  $\hat{r}_0 = 6M$ ,  $\hat{\sigma} = M$ ,  $M\mu = 0.4$ , the Proca field settles to a stable configuration after  $t \sim 500M$  of evolution time, as shown in Fig. 2. The field normal component  $\Phi'$  and dark magnetic field  $\vec{B}'$  within  $r < 20M$  approximately follow  $\ell = m = 1$  spherical harmonics ( $\ell, m$  understood as the usual angular and azimuthal numbers for spherical harmonics). This agrees with the perturbation calculation, where the dominant mode confined near black hole is  $n = 0, m = 1, S = -1$  mode (the overtone, azimuthal, polarisation numbers for FKKS formulatiuon [36–38]), whose angular distribution overlaps mostly with  $Y_{11}$  spherical harmonics.

After the dark photon cloud is formed, it decays outward through emission of (gravitational and dark electromagnetic) radiation. We will find it useful to analyze this decay in terms of Newman-Penrose (NP) formalism. We set up the null tetrad  $(k^\mu, l^\mu, m^\mu, \bar{m}^\mu)$  by

$$\begin{aligned} k^\mu &= \frac{1}{\sqrt{2}}(\hat{n}^\mu - \hat{r}^\mu), \\ l^\mu &= \frac{1}{\sqrt{2}}(\hat{n}^\mu + \hat{r}^\mu), \\ m^\mu &= \frac{1}{\sqrt{2}}(\hat{\theta}^\mu + i\hat{\phi}^\mu), \end{aligned} \quad (39)$$

where  $\hat{n}$  is the unit vector in the normal  $n^\mu$  direction, and  $(\hat{r}, \hat{\theta}, \hat{\phi})$  is a basis of orthonormal spatial vectors which asymptotically behave as radial, polar and azimuthal vectors. The

NP scalar of spin weight -1 for Proca field is (not to confuse with the notation for time component of electromagnetic field)

$$\phi_1 = \frac{1}{2} F'_{\mu\nu} (l^\mu k^\nu + \bar{m}^\mu m^\nu). \quad (40)$$

Different multipoles of  $\Phi_1$  can be extracted by expansion

$$\phi_1 = \sum_{\ell, m} \phi_1^{\ell m} Y_{\ell m}. \quad (41)$$

In our case, the dominant multipole is  $(1, 1)$  mode  $\phi_1^{11}$ . The  $(1, 1)$  mode of Proca NP scalar of spin weight 0 is shown in the lower panel of Fig. 2. It follows a  $-5/6$  power law decay at late times, as expected from perturbative calculations. Similar power law decays have also been observed by Ref. [40].

Higher order modes are present in our setup of the Proca field, which will play an important role in interaction with the visible sector. The dominant  $n = 0, m = 1, S = -1$  mode is confined near the horizon and exponentially decays with a characteristic radius  $r \sim M/\mu^2$ . This agrees with our simulation within around  $r < 10M$  for  $\mu M = 0.4$  as shown in upper panel of Fig. 3, as well as results in early simulations [41, 42]. Perturbation calculations [37] show subdominant modes of  $S = +1$  polarisation are centered further away from the black hole, and will be important in its interaction with accretion disks and winds at large radii. Our simulations have physical extent of  $x = \pm 1024M$  and include the subdominant modes.

#### D. Numerical implementation

Having outlined the mathematical description of the coupled Einstein-Proca-GRMHD (dark magnetohydrodynamics) system we are solving, we will now describe the numerical framework and setup used to carry out the simulations presented in subsequent Sections.

Our simulations make use of various codes based on, or provided by the Einstein Toolkit [103]. The Proca sector is solved using the publicly available suite of Canuda codes [40, 104, 105], suitably modified for coupling them with a GRMHD evolution. In particular, we discretize the system using fourth-order finite differencing with Kreiss-Oliger dissipation. The use of unlimited finite-difference approaches is appropriate since the turbulent dynamics of the matter does not appreciably backreact on the dark photon cloud itself. The GRMHD equations are solved using the Frankfurt/IllinoisGRMHD (FIL) code [106, 107]. FIL provides a fourth-order accurate discretization of the GRMHD equation in vector potential form [108]. On the technical side, the equations are solved using a modified ECHO scheme [109], with WENO-Z reconstruction and improved primitive recovery [102], as used in recent GRMHD studies performed with FIL [110–114]. Due to the coupling with the Proca field, we needed to modify the primitive recovery method of Ref. [102]. A detailed description is provided in Appendix B.

The spacetime is evolved using the Antelope module in FIL in the Z4c formulation [115, 116]. We adopt moving



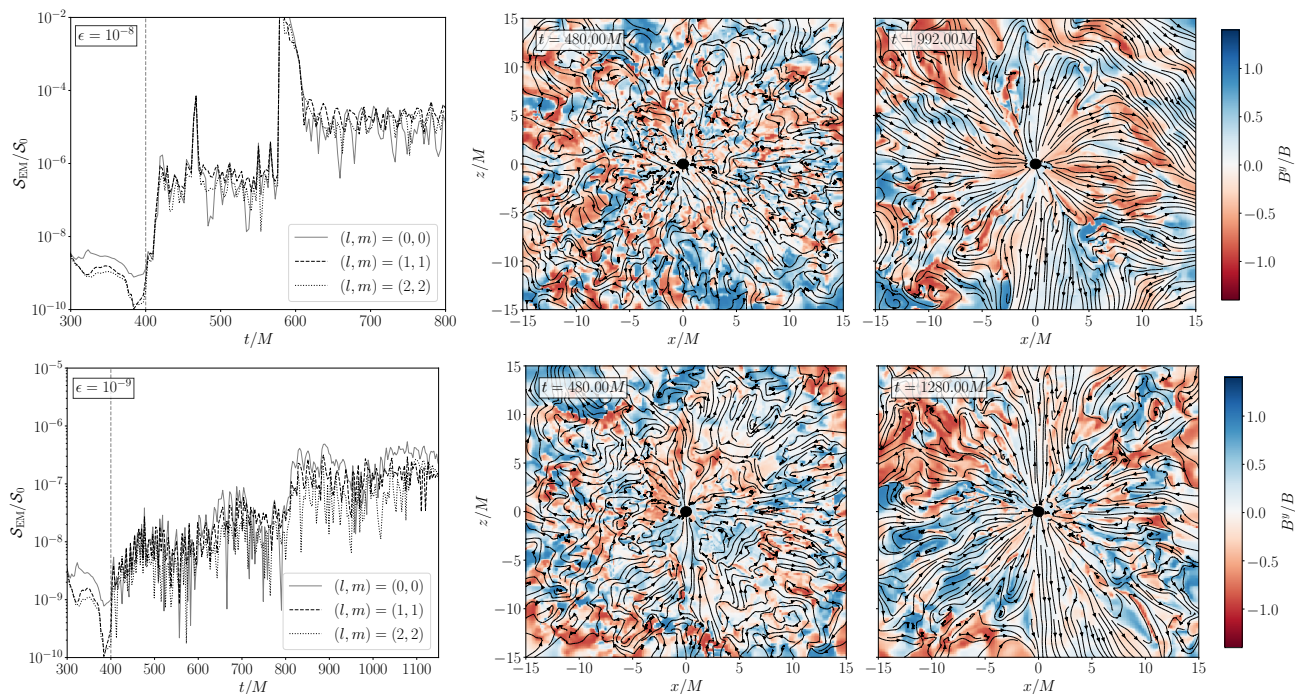


FIG. 4. Electromagnetic energy (Poynting) flux sourced by the dark photon cloud (*left*) and magnetic field configurations in the growth (*middle*) and saturation stage (*right*). Coupling constants are set to  $\epsilon = 10^{-8}$  (top) and  $\epsilon = 10^{-9}$  (bottom). As discussed in the main text, the Poynting scalar  $\mathcal{S}_{\text{EM}} = (\vec{E} \times \vec{B}) \cdot \hat{r}$  is shown relative to  $\mathcal{S}_0 = 10^{-16} M^{-2}$ , where  $M$  is the black hole mass. Shown is the strength of the out-of-plane magnetic field component,  $B^y$ , relative to the total field strength,  $B$ . Solid/dashed/dotted curves are  $(0, 0)/(1, 1)/(2, 2)$  modes of Poynting scalar extracted at radius  $r = 10M$ . Vertical dash lines mark the time coupling is switched on ( $t = 400M$ ). The streamlines on middle and left panels are visible magnetic field lines projected on the meridional plane.

puncture gauges [117], and discretize the equations using a fourth-order accurate finite-difference scheme [118].

The simulations were performed using the `EinsteinToolkit` infrastructure [119] with adaptive mesh-refinement provided by the `Carpet` code [120].

In detail, we adopt the following grid setup: Our simulation uses a 3D Cartesian grid with 9 static mesh refinement levels. The physical domain extends to  $-1024 < x_i/M < 1024$  in all directions. The resolution doubles at each refinement level with the finest grid spacing being  $\Delta x = 0.04M$ . The initial spin parameters are set to  $a = 0.9$  for a highly spinning spacetime background. The initial spacetime is set by solving the puncture equation in the presence of a Proca field [40, 121], using the `Canuda` code [122].

#### IV. RESULTS

With our numerical implementation of the dark GRMHD system, interactions between the dark photon cloud and various astrophysical environments can be simulated. As a first test and application, we focus on black hole accretion in two different regimes. First, we consider a regime where the black hole is embedded in a low density gaseous environment, which is dominated by the dark field,  $A_\mu \ll \epsilon A'_\mu$  (Sec. IV A). Second, we consider an advection dominated accretion flow [123, 124], where the dark photon field is subdominant to the

visible magnetic field governing the accretion flow  $A_\mu \geq \epsilon A'_\mu$  (Sec. IV B).

In all of the flows we consider, we assume a mass hierarchy, in which the fluid is not self-gravitating, the fluid motion does not affect the decay and dynamics of the dark photon cloud. In this way, the dark photon cloud has a mass scale relative to the black hole mass, and the fluid only acquires a mass scale through the mixing constant we choose.

Because the fluid quantities are much smaller than the gravitational scale set by black hole mass  $M$ , for numerical accuracy, we rescaled the magnetic fields and mass densities by small units of  $B_0 = 10^{-8} M^{-1}$  and  $\rho_0 = 10^{-16} M^{-2}$ . The coupling constants we explored are around  $10^{-9} < \epsilon < 10^{-7}$  and the stable configurations of dark photon cloud has  $A'_\mu \sim 10^{-3}$ . The frequency of the dark photon cloud is of order  $\omega_R \sim \mu = 0.4M^{-1}$ . As estimated by Eq. 9, influence of such dark photon field corresponds to a visible magnetic field at order  $10^{-11} M^{-1} \sim 10^{-9} M^{-1}$ . In the simulations presented in this paper, we explore two scenarios, the black hole with low density, low magnetization gas at order  $B \sim 10^{-5} B_0$  where the dark photon cloud dominates the interaction, and the accretion disk with magnetic field in jet region of order  $B \sim B_0$  where the dark photon cloud appears as a perturbation to MHD quantities.

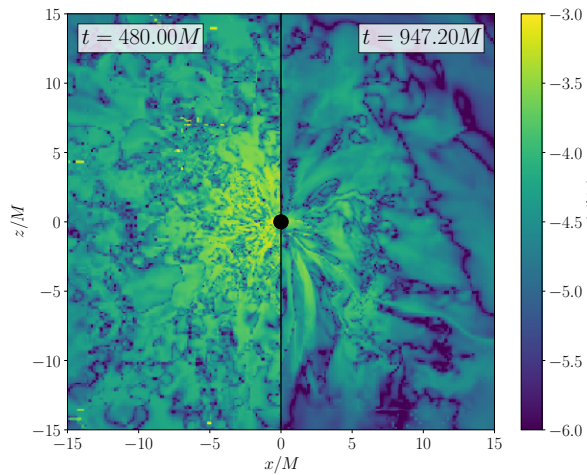


FIG. 5. Effective  $\alpha$  dynamo-term in the Ohms law for the force-free like isolated BH simulations. Shown are early and late times for the  $\epsilon = 10^{-8}$  simulation shown in Fig. 4.

### A. Black holes in low density nearly force-free environments

As a first step, we consider the evolution of a black hole in a low density force-free gas. Taking the limit of a dominant dark photon cloud, we can consider the scenario where the dark photon cloud will drive the generation of visible magnetic field and dynamics of the plasma via the dark Lorentz force and dynamo terms. Such a scenario has been recently considered by Ref. [60] using dark force-free electrodynamics. In the limit of high magnetization  $\sigma = b^2/\rho \gg 1$  our simulations are able to reproduce this limit, though in general subtle differences exist, including the potential for shock formation [114].

The initial condition is motivated by a Wald scenario commonly studied for pair plasmas [125, 126]. We initialize the system with vertical magnetic field,  $B_z \ll \epsilon\Phi'$ . If sufficiently magnetized, such that the system reaches a nearly force-free state, such a solution on its own will form a transient jet-like outflow by accreting vertical flux on the black hole. Instead, here we consider a case of low magnetization,  $\sigma = 0.01$ , for which accretion of plasma will largely be hydrodynamical. That is, without additional amplification of magnetic fields, which needs to be provided by an external energy reservoir, the system would not (on the timescales we consider here) become magnetically dominated or launch any outflows. As we will now show, energy conversion of the superradiant cloud into the magnetic field is able to drastically change this picture, as initially demonstrated by Ref. [60].

After turning on the coupling, the dark photon field will interact with the magnetic field around the black hole and begin to amplify the field. We can see that initially at time  $\Delta t = 80M$  after the coupling was turned on the field begins to get turbulently amplified (see Fig. 4). A similar observation was also made by Ref. [60]. At later times, we can see that the magnetic field rearranges itself into a Wald like structure, around

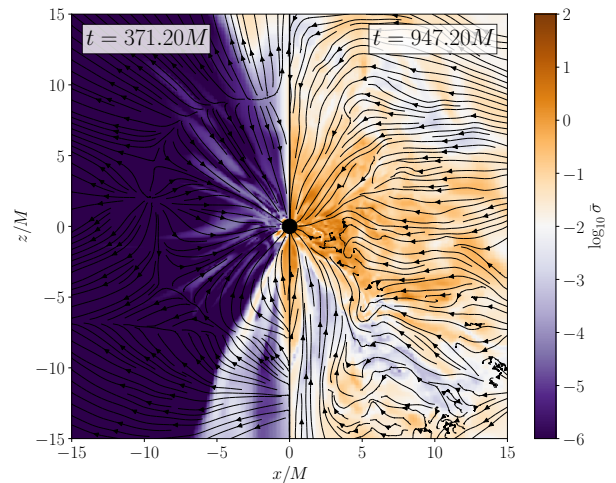


FIG. 6. Magnetization parameter  $\sigma = b^2/\rho$  for the strong coupling case  $\epsilon = 10^{-8}$ . Streamlines include the velocity structure of the gas flow. The simulation is the isolated BH solution shown also in Fig. 4.

the black hole with large scale flux tubes emerging. This ordered field structure seems to settle into a constant outflow state as indicated by the Poynting flux measured close to the hole (Fig. 4). Overall, the dark photon cloud itself does not imprint its oscillation modes onto the Poynting flux, as multiple modes are present and of comparable strength. The coupling strength of the dark photon to the visible photon clearly impacts the amount of larger structure formation, with more large scale structures being present for the stronger coupling case ( $\epsilon = 10^{-8}$ ). We can best quantify this effect by consider the dark contribution to the induction equation, which in the near ideal MHD regime we consider governs the evolution of the magnetic field. We find that, expressed as an  $\alpha$ -term,  $A^\mu b_\mu/b^2$ , the system features substantial and strong contributions at early times. These drive turbulent dynamo amplification of the magnetic field in the vicinity of the black hole, which switches off at late times, with the magnetic field lines being largely perpendicular to the dark vector field  $A^\mu$ . In addition, we quantify this saturated state also in terms of the magnetization  $\sigma$ , as shown in Fig. 6. Here, we can see that at late times the close vicinity of the black hole is in a nearly force-free state  $\sigma > 1$ . Velocity streamlines indicate that increased accretion onto the black hole.

### B. Black hole accretion

We now focus on the case of an accretion disk around a spinning black hole commonly used to model accretion around compact objects [127]. We initialize the dark photon field as before, but this time add a constant angular momentum torus with a vertical net magnetic fields of magnitude  $B_z \gg \epsilon\Phi'$ . In this case, the flow structure will only be perturbatively affected by the Proca field, different from the case considered in the previous section. We expect such a scenario to be more realistic given that dark matter should only couple

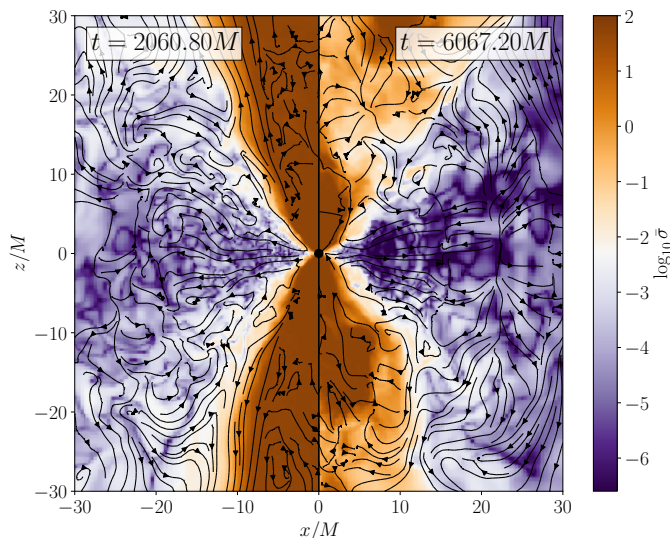


FIG. 7. Fluid velocity streamlines and distribution of magnetization  $\sigma = b^2/\rho$  for the accreting black hole scenario. The time,  $t$ , is shown relative to the start time of the simulation, where  $M$  is the black hole mass. We activate the dark photon coupling once a quasi-steady state is reached corresponding roughly to the time shown in the left panel.

weakly to accretion flows.

To obtain a quasi-equilibrium configuration of an accretion disk, the hydrodynamic quantities need to be correctly set in the initial condition to have a stable circulation of fluid around black hole. Due to the non-negligible self-gravity of the dark photon cloud, the spacetime is not that of a Kerr black hole, but gets modified. We, therefore, adopt the solution of a hydrodynamic equilibrium disk in general spacetimes by Abramowicz-Jaroszynski-Sikora (AJS) [128] as our initial condition, which is parametrized by the specific angular momentum  $l_{\text{AJS}}$  in the disk, and energy potential  $W_{\text{in}}$  at inner edge. More details on the initial configuration are given in Appendix C.

In this set of simulations, we rescaled the MHD quantities for numerical accuracy, so that the magnetic field is in units of  $B_0 = 10^{-8} M^{-1}$  and relative densities are normalized by  $\rho_0 = 10^{-16} M^{-2}$ . In cgs units, for an  $M = 10^9 M_\odot$  supermassive black hole,  $B_0 \approx 235$  Gauss and  $\rho_0 \approx 6 \times 10^{-17} \text{g/cm}^3 \approx 3.4 \times 10^{10} m_e/\text{cm}^3$ . In the simulations we present, the maximum magnetic field near the jet region is around  $0.1 B_0$  and the maximum density inside the disk is around  $0.5 \rho_0$ .

The system we simulate features a simple advection dominated accretion flow, which does not become magnetically arrested [129]. The accretion flow can roughly be split into a jet and disk region, as can be seen from the magnetization  $\sigma$  (see Fig. 7). The background accretion state is shown in the left most panel of Fig. 9. We evolve the system into a quasi-steady accretion state as indicated by a constant mass accretion rate,  $\dot{M}_{\text{BH}}$ . While different accretion states could be considered, these are typically more dynamical and can feature periodic eruptions [129, 130], which may make an initial analysis of potential dark matter effects harder to quantify.

After enabling the dark photon coupling, we evolve the ac-

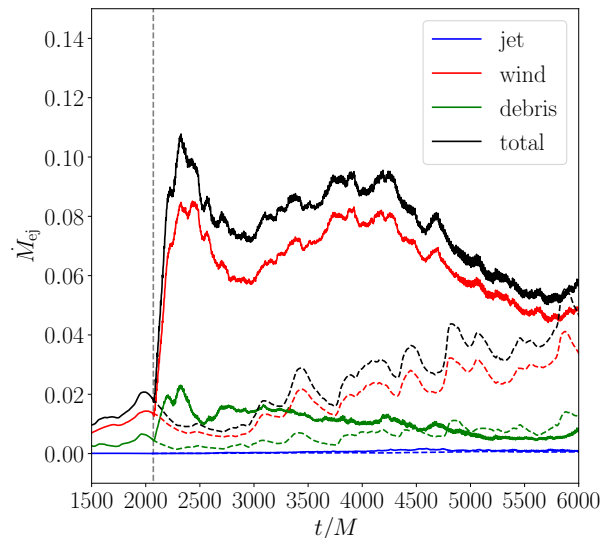


FIG. 8. Coupling to the dark photon cloud enhances the outflow rate,  $\dot{M}_{\text{ej}}$  (top, measured at  $r = 90M$ ), while the accretion rate was not significantly changed (bottom, measured at  $r = 3M$ ). Contributions to the outflow: Jet region (blue, integrated  $10^\circ$  around  $z$ -axis), debris stream (green, integrated  $10^\circ$  above and below equatorial plane), and disk wind (red, integrated between the jet and debris boundaries).

creted system into a new quasi-steady state. We point out that for the couplings and mass hierarchies we explore, the dark photon cloud never dominates the accretion flow as it does in the previous Section. Consequently, the effects we probe by construction will largely act as corrections/perturbations to the background flow.

We quantify the impact of the dark photon field in different ways. First, we aim to quantify the impact on the standard model magnetic field, as well as on the energy transfer between the plasma and the cloud.

In the accretion disk simulations we study in this work, only the effect of the dark Lorentz force, controlled by coupling constant  $\epsilon$ , is turned on, while the dynamo-like effect in Eq. 23, controlled by the rescaled coupling  $\bar{\epsilon}$ , is effectively not included, i.e. the simulations are in the ideal limit with perfect conductivity. This is because the dominant effect in this accretion state will be the dark Lorentz force. In line with our previous discussion, we justify this assumption by a posteriori estimating an effective  $\alpha$ -term in the induction equation, which is given by  $\kappa b^t$  (see e.g. [113, 131]) with  $\kappa \sim A_i b^i / b$ . This is shown in the center row of Fig. 9. We see the effect is weak inside around  $r \sim 10M$  where most cloud energy resides.

We can see that the impact of this term scales with the coupling, with stronger couplings providing substantial corrections to the electromotive force. Due to alignment of the magnetic field with the dark photon field, the effect is suppressed in the close vicinity of the black hole, and (where matter-free) also in the jet region. The strongest injection seemingly takes place in low density regions, with the effect being of comparable order throughout the accretion disk, but at least one order lower than in Fig. 5, where the effect was more substantial



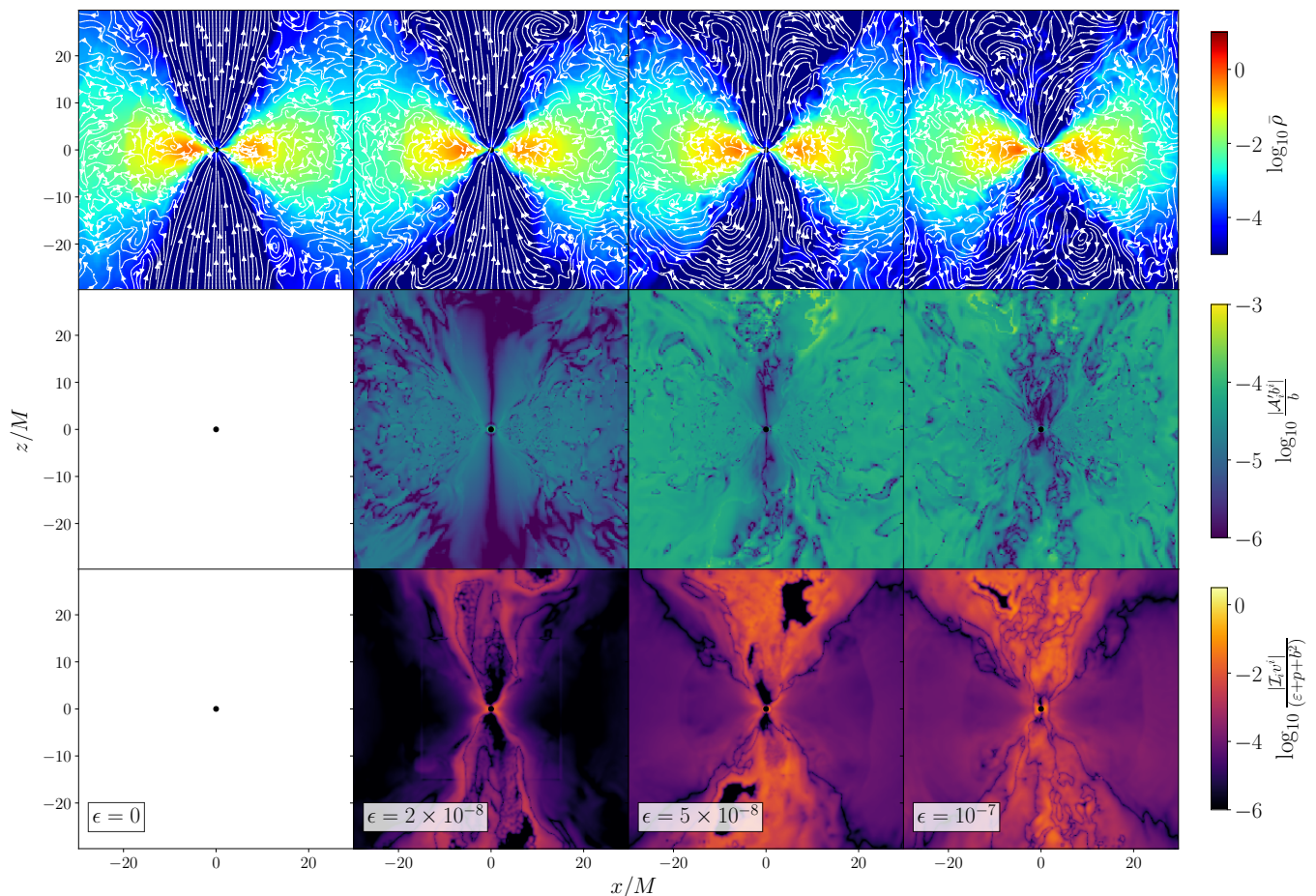


FIG. 9. Influence of dark photon on accretion disks at different coupling strength  $\epsilon = 0, 2 \times 10^{-8}, 5 \times 10^{-8}, 10^{-7}$  at a late time  $t = 6016M$  after the coupling is turned on at  $t = 2070M$ , where  $M$  is the black hole mass. Top row: fluid density normalized by reference  $\rho_0 = 10^{-16}M$  and visible magnetic field lines  $\vec{B}$  shown in white. Middle row: magnitude of fluid magnetization  $\sigma = b^2/\rho$  and velocity streamlines. Bottom row: dark Ohmic heating rate,  $I^i v_i$  acting on the fluid normalized by  $(\epsilon + p + b^2)$ .

and dynamically important.

In addition to changes to the induction equation, the dark Lorentz force can also act on the accretion flow. We quantify this effect by computing the effective dark heating term  $I_i v^i$  (bottom row, Fig. 9). Looking at different coupling strengths, we can see that the impact on the disk is always subdominant, however in the jet sheath region, as well as in the funnel for higher couplings we see up to 10% energy injection rate relative to the enthalpy,  $\epsilon + p + b^2$  of the fluid. This leads us to speculate that the impact on low density regions is likely strongest in this context.

We now briefly review some global properties of the accretion flow. For the disk properties, we further quantify the influence of the dark sector on the outflow, accretion rate, oscillation modes, and the magnetic flux threading the black hole (see Fig. 10). We begin with the mass outflow/ejection rate,  $\dot{M}_{\text{ej}}$ , which we measure on a spherical surface at a distance  $r = 90M$  from the black hole. We can see that the outflow rate is roughly constant for most of the simulation without dark photon coupling. Once the coupling is turned on, especially in the wind region, the outflow is significantly en-

hanced, increasing by one order of magnitude. We further quantify where this outflow is sources by looking at projections in various azimuthal bins (see Fig. 8). We can clearly see that jet and equatorial outflows are unaffected by the dark photon field. Instead, the main effect is driving a wind (likely from the disk edge) where we found the energy injection from the dark cloud to be substantial (see Fig. 9). Overall, the amount of outflows scales with the coupling, but not very strongly so, with variations in the outflow rate due to changes in  $\epsilon$  being less than a factor three. Also, both Fig. 8 and 10 show that the outflow saturates after  $\sim 500M$  time of coupling with the dark sector, and enters a relatively stable stage where the dynamics are altered by Proca field. We can contrast this behaviour with the mass accretion rate on the black hole,  $\dot{M}_{\text{BH}}$ . Consistent with the absence of modifications in the jet region, the mass accretion rate onto the black hole seems entirely unaffected by dark photon interactions. This lets us draw the important conclusion that likely jet luminosities (in the coupling regimes we consider) will not be affected by the dark photon field. Consistent with this assessment, the magnetic flux on the black hole  $\Phi_{\text{BH}} = \int |B^r| \sqrt{-\gamma} d\Omega$  neither decreases nor increases due to



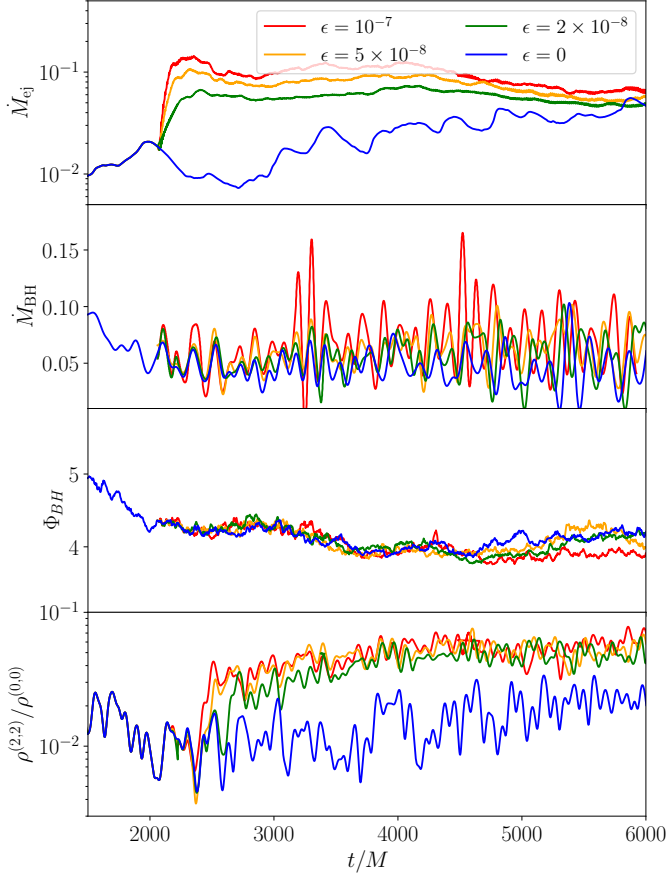


FIG. 10. Shown are: Mass outflow rate  $M_{\text{ej}}$  across the surface at  $r = 90M$  for different coupling constants  $\epsilon = 10^{-7}$  (red),  $5 \times 10^{-8}$  (orange)  $2 \times 10^{-8}$  (green), and no coupling for reference (blue), the mass accretion rate,  $\dot{M}_{\text{BH}}$  and the magnetic flux  $\Phi_{\text{BH}} = \int |B^r| \sqrt{-\gamma} d\Omega$  across the surface near horizon at  $r = 3M$ , the  $(\ell, m) = (2, 2)$  harmonic oscillation modes of fluid density,  $\rho$  extracted at  $r = 10M$ . All times,  $t$ , are stated relative to the mass  $M$  of the black hole.

the presence of a dark photon coupling. Meaning that regions close to the black hole, where the standard model magnetic field will be strongest, are indeed unaffected. Finally, we do observe bar shaped disk oscillations driven by the decaying Proca field in the disk, as quantified by the  $l = m = 2$  mode of the rest-mass density in the disk. However we caution that the oscillation strength seems independent of the coupling, and the change is less than a factor 2 compared to the no coupling case, making the effect potentially subleading.

Having found that the dark Lorentz force alters the wind ejection, we now attempt a more detailed assessment of hydromagnetically driven wind properties. To this end, we perform an analysis commonly used for protoplanetary disks (e.g., [132]).

The dark Lorentz force  $\vec{J}$  continues to drive the evolution of accretion disks in the wind region at late times. When the coupling to the dark photon is absent, dynamics of disk wind can be well-approximated by the analytic solutions of Blandford-Payne process for axisymmetric flows [88]. In a steady state,

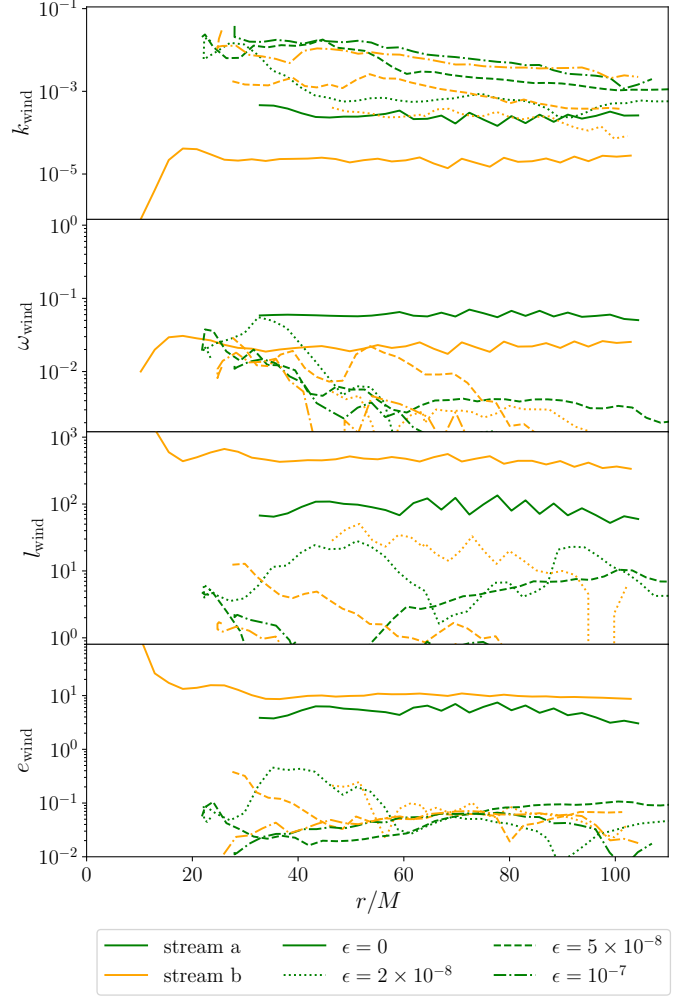


FIG. 11. Conserved wind quantities along the the yellow and green streamline shown in Fig. 12. These include the mass loading parameter  $k_{\text{wind}}$ , the effective rotation rate  $\omega_{\text{wind}}$ , the specific angular momentum  $l_{\text{wind}}$ , and the Bernoulli energy density  $e_{\text{wind}}$ . Dashed lines indicate simulations with non-zero dark photon coupling  $\epsilon$ . We can see that in the presence of a dark matter coupling, especially the rotation quantities,  $\omega_{\text{wind}}$  and  $l_{\text{wind}}$ , are no longer conserved.

the fluid streams follow magnetic field lines in the wind region and there are four conserved quantities along the field lines[133, 134]

$$k_{\text{wind}} = \frac{\rho v_p}{B_p}, \quad (42)$$

$$\omega_{\text{wind}} = \frac{v_\phi}{R} - \frac{B_\phi v_p}{B_p R}, \quad (43)$$

$$l_{\text{wind}} = R \left( v_\phi - \frac{B_\phi}{k_{\text{wind}}} \right), \quad (44)$$

$$e_{\text{wind}} = \frac{v^2}{2} + h + \Phi_g + \frac{B_\phi^2}{\rho} - \frac{B_\phi v_\phi}{k_{\text{wind}}}, \quad (45)$$

where the velocity and magnetic field are decomposed into poloidal and toroidal components  $\vec{B} = \vec{B}_p + B_\phi \hat{\phi}$ ,  $\vec{v} = \vec{v}_p + v_\phi \hat{\phi}$

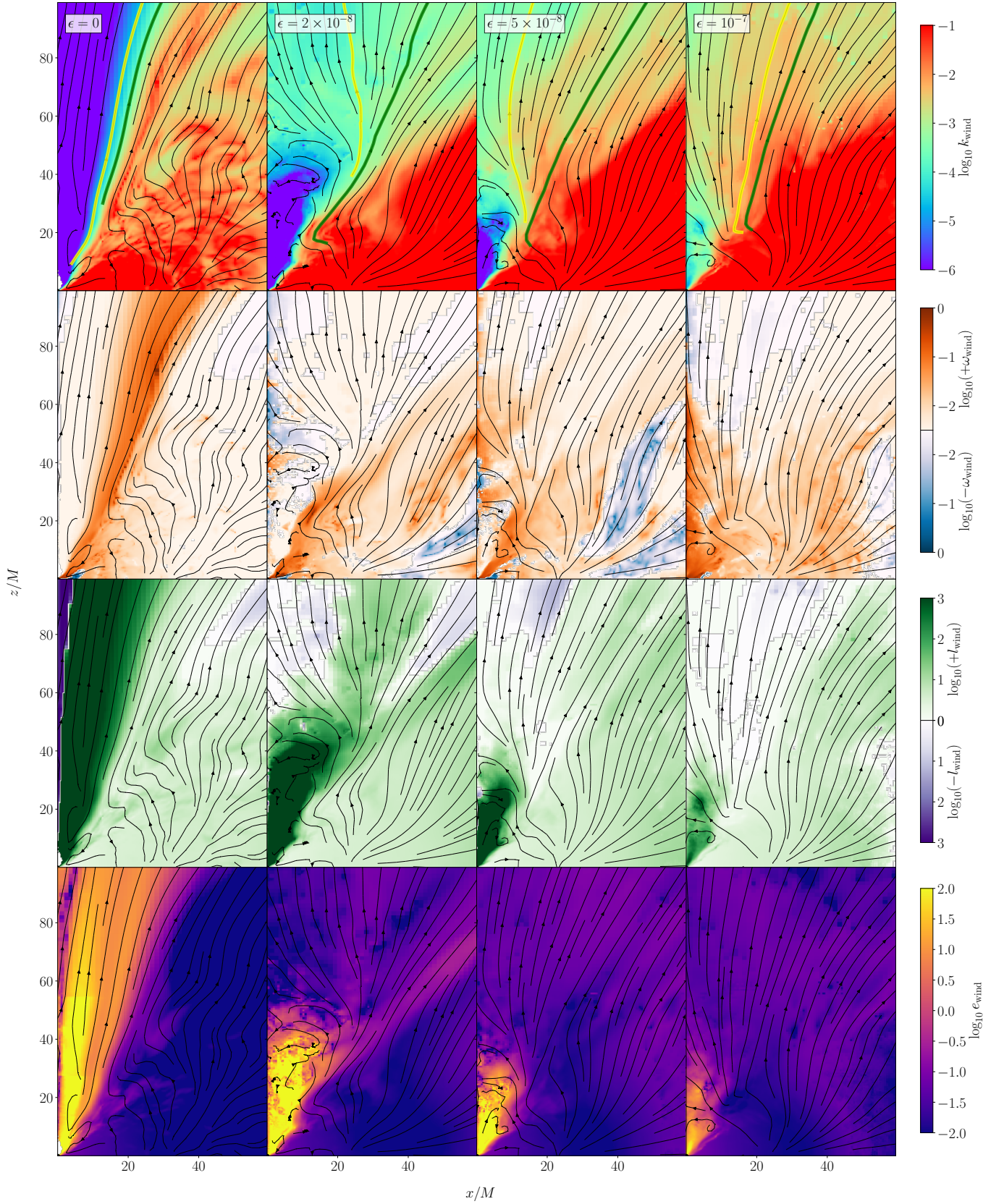


FIG. 12. The conserved quantities in the wind region for different coupling strengths, averaged over time  $4857.6M < t < 5216.0M$ , where  $M$  is the black hole mass. The velocity (black) streamlines are shown for reference. In the case with no coupling (first column),  $k_{\text{wind}}$ ,  $\omega_{\text{wind}}$ ,  $l_{\text{wind}}$ ,  $e_{\text{wind}}$  are approximately conserved along fluid streams, i.e. velocity streamlines appear as equipotential contours. However, when the coupling is turned on ( $\epsilon = 2 \times 10^{-8}$ ,  $5 \times 10^{-8}$ ,  $10^{-7}$ , in second, third and fourth columns), the wind quantities are no longer conserved along fluid streams. We quantify this in Fig. 11 by tracing the conserved quantities along the streams highlighted by thick yellow/green lines on the top panels.

on a cylindrical coordinate  $(R, \phi, z)$ .

Using this formalism, we can quantify whether or not additional outflows will be dark matter driven, since the presence of a dark Lorentz force will alter the conserved quantities. The dark sector acts as an external supply of energy and angular momentum, so that the combined system does not satisfy the simple symmetries of the Blandford-Payne process. While in principle, a full derivation of the wind quantities in the presence of a dark photon field could be done (assuming the dark photon cloud is approximately axisymmetric), we forgo such an approach in this initial work, and limit ourselves by showing that including dark matter effects leads to a non-conservation especially of the rotational quantities.

We assess the validity of this approach, by choosing two streamlines (highlighted in green and yellow colors in Fig. 12). We then compute the various conserved quantities for cases with and without coupling to the dark photon field, which we show in Fig. 11. By considering a case without coupling, we establish the baseline degree to which our code can conserve the wind quantities. This is shown with solid lines in Fig. 11. We observe that conservation holds extremely well for all quantities along their respective fluid streamlines. In numerical simulations of accretion disks, it is also observed that the four quantities above are conserved along fluid streams in a statistical sense after a time/azimuthal average [132, 135]. We have also confirmed this in the fiducial simulation with no coupling to dark sectors.

We now perform the same analysis for similar streamlines in the simulations with active coupling,  $\epsilon > 0$ . In this case, the standard model Lorentz force gets supplemented with its dark equivalent altering the force balance of the system.

We observe that with coupling enabled the mass loading parameter  $k_{\text{wind}}$  increases by at least one order of magnitude. Consistent with the observation that substantial disk winds are present in those simulations. We can also nicely see this by looking at a spatial distribution of  $k_{\text{wind}}$  in Fig. 12. We can see that with enabled coupling the wind launching increases mass loading everywhere with clear break outs from the disk visible. This effect increases monotonically with the coupling parameter  $\epsilon$ .

We can further see that the energy density,  $e_{\text{wind}}$ , is well conserved, albeit with a substantial offset compared to the non-coupled simulation indicating that we are consistently missing out on an energy contribution from the dark photon cloud. Indeed, we already saw in Fig. 9, the energy transfer between the dark and visible sectors is particularly strong on surfaces of the disk.

The main difference is associated with the enhanced wind launching, namely the change in specific angular momentum  $l_{\text{wind}}$ .

The modes of superradiant dark photon around highly spinning black holes are of high angular momentum, having the largest overlap with spherical harmonic  $\ell = m = 1$  mode. In other words, the dark Lorentz force highly modifies the toroidal part of the force. Therefore, the angular quantities  $\omega_{\text{wind}}$ ,  $l_{\text{wind}}$ , shown in the second and third rows, are changed by several orders of magnitude. Some streams even go counter-rotating at large radii. In Fig. 12, we see a layer of

anti-rotating streams, with opposite sign of angular  $\omega'_{\text{wind}}$  and  $l'_{\text{wind}}$ . This is driven by the dark Lorentz force in the toroidal direction. The dark magnetic field is mostly in poloidal direction  $\vec{B}' \approx \vec{B}'_p$ . On a mathematical level, the interaction alters the magnetic field configuration so that the vector potential has nonzero poloidal component  $\vec{A}_p \neq 0$ , thus generating a force in the toroidal direction  $\epsilon\mu^2 \vec{A}_p \times \vec{B}'_p$  which alters the angular quantities. Overall we find a strong reduction of  $l_{\text{wind}}$  with increasing dark photon coupling strength.

## V. CONCLUSION

In this work we have numerically investigated the potential impact of a superradiant dark photon cloud on different black hole accretion flows. Superradiance, originally proposed from black hole perturbation theory calculations [31] and recently further corroborated by numerical simulations [39, 41, 42], has been the prominent feature of massive bosonic fields around spinning black holes. As a first series of simulations based on our formulation, we studied the field configuration, energy distribution and decay curves of cloud total energy and vector field radiation during the evolution of dark photon cloud in the presence of astrophysical accretion flows. We have done so in several steps. First, we have derived a formulation of the coupled Einstein, Proca and GRMHD (dark magnetohydrodynamics) systems in the nearly perfectly conducting limit. The resulting system retains a dark Lorentz force and a dynamo-like modification of the induction equation, through which the massive dark photon (Proca) evolution can feedback on the plasma. This dark magnetohydrodynamics system was then implemented into a full 3+1 numerical relativity code (based on the EinsteinToolkit[119], Canuda[136], and FIL [106]).

We have then numerically solved the dark magnetohydrodynamics system for two different black hole accretion flows in the presence of a dark photon cloud. First, we have focused on a case where the dark photon cloud drives accretion in a nearly force-free plasma, similar to a case considered by Ref. [60]. We found that the dark photon cloud can substantially drive magnetic field amplification and alter the structure of the accretion flow via the dark Lorentz force. In the main part of our work, we have considered a simple advection dominated accretion flow onto a supermassive black hole. In this scenario, we have investigated the potential impact of the dark photon cloud onto the flow. We found that the dark cloud will mainly act on the flow via the dark Lorentz force, driving oscillations and outflows from the disk. We also confirmed by means of a detailed wind analysis following Refs.[88, 132], that especially the angular velocity of the wind is directly impacted by the dark Lorentz force. This leads us to speculate that wind outflows and potential X-ray signatures from the disk surface may be impacted.

Overall, this work is intended as a first demonstration of the general-relativistic dark magnetohydrodynamic framework. As such, we have limited ourselves to an idealized accretion scenario. One of the key objectives of using our framework is to provide potential actual signatures of superradi-

ant dark photon clouds. Potential applications could be studies of low luminosity accretion flows observable comparable to those observable with the Event Horizon Telescope [137–139]. These will require studies of a magnetically arrested regime [129], which we have not considered here. Other applications could be stellar mass mergers in AGN disks [140, 141], for which potential interactions with the flow and jet launching from the black hole may be relevant. Such a scenario (without gaseous accretion flows) has been speculated earlier to results in additional X-ray signatures [60]. Super-radiance around binary systems is also shown to be possible [142], and may affect circumbinary disk accretion flows [143].

### ACKNOWLEDGMENTS

The authors are grateful to W. East, J. Huang and A. Philippov for insightful discussions. Simulations were performed on the Sherlock clusters at Stanford University. SX acknowledges support by US Department of Energy under contract DE-AC02-76SF00515. ERM acknowledges support by the National Science Foundation under grants No. PHY-2309210 and AST-2307394, as well as on the NSF Frontera supercomputer under grant AST21006, and on Delta at the National Center for Supercomputing Applications (NCSA) through allocation PHY210074 from the Advanced Cyberinfrastructure Coordination Ecosystem: Services & Support (ACCESS) program, which is supported by National Science Foundation grants #2138259, #2138286, #2138307, #2137603, and #2138296.

### Appendix A: 3+1 decomposition of fluid equations with external energy-momentum flux

Eq. 30, 31 follows from similar derivations for 3+1 decomposition of energy-momentum conservation in most textbooks[97]. We first list some useful properties that are repeatedly used:

$$\nabla_\mu n_\nu = -K_{\mu\nu} - n_\mu D_\nu \ln \alpha, \quad (\text{A1})$$

$$\nabla_\mu n^\mu = -K, \quad (\text{A2})$$

$$n^\mu \nabla_\mu n_\nu = D_\nu \ln \alpha, \quad (\text{A3})$$

$$\sqrt{\gamma}^{-1} \partial_t \sqrt{\gamma} = D_j \beta^j - \alpha K, \quad (\text{A4})$$

$$D_j Q_i^j = \sqrt{\gamma}^{-1} \partial_j (\sqrt{\gamma} Q_i^j) - \Gamma_{ij}^k Q_k^j, \quad (\text{A5})$$

with  $Q$  an arbitrary (1,1) tensor and  $\Gamma_{ij}^k = \frac{1}{2} \gamma^{k\ell} (\partial_i \gamma_{\ell j} + \partial_j \gamma_{\ell i} - \partial_\ell \gamma_{ij})$  the Christoffel symbol corresponding to spatial metric.

#### 1. Energy equation

Projecting the equations on  $n^\nu$  and expand  $T_\nu^\mu$  we get

$$\begin{aligned} -\mathcal{I}_\phi &= n^\nu \nabla_\mu T_\nu^\mu, \\ &= n^\nu \nabla_\mu S_n^\mu u + n^\mu n^\nu \nabla_\mu S_\nu - \nabla_\mu S^\mu + KS - n^\mu \nabla_\mu S, \end{aligned} \quad (\text{A6})$$

Using  $S_\nu^\mu n^\nu = 0$  and  $n^\nu S_\nu = 0$ , we have

$$n^\nu \nabla_\mu S_\nu^\mu = -S_\nu^\mu \nabla_\mu n^\nu = K^{\mu\nu} S_{\mu\nu}, \quad (\text{A7})$$

$$n^\mu n^\nu \nabla_\mu S_\nu = -n^\mu S_\nu \nabla_\mu n^\nu = -S_\nu D^\nu \ln \alpha, \quad (\text{A8})$$

and the 4-divergence can be expressed by spatial covariant derivatives

$$\nabla_\mu S^\mu = D_\mu S^\mu + S^\mu D_\mu \ln \alpha. \quad (\text{A9})$$

Together with Eq. A6 we obtain

$$\partial_t S - \beta^i D_i S + \alpha (D_\mu S^\mu - KS - K^{\mu\nu} S_{\mu\nu} - \mathcal{I}_\phi) + 2S^\mu D_\mu \alpha = 0. \quad (\text{A10})$$

To rewrite this into flux-conservative form, we collect

$$\partial_t S - D_i (\beta^i S - \alpha S^i) + S D_i \beta^i - \alpha KS - \alpha K^{ij} S_{ij} - \alpha \mathcal{I}_\phi + S^i D_i \alpha = 0, \quad (\text{A11})$$

and use  $D_i (\beta^i S - \alpha S^i) = \sqrt{\gamma}^{-1} \partial_i [\sqrt{\gamma} (\beta^i S - \alpha S^i)]$ ,  $D_j \beta^j - \alpha K = \sqrt{\gamma}^{-1} \partial_t \sqrt{\gamma}$ , we finally arrive at

$$\begin{aligned} \partial_t (\sqrt{\gamma} S) - \partial_i [\sqrt{\gamma} (\beta^i S - \alpha S^i)] \\ = \sqrt{\gamma} [\alpha K^{ij} S_{ij} - S^i D_i \alpha + \alpha \mathcal{I}_\phi]. \end{aligned} \quad (\text{A12})$$

#### 2. Momentum equations

We have

$$\gamma_\alpha^\nu \nabla_\mu S_\nu^\mu - KS_\alpha + \gamma_\alpha^\nu n^\mu \nabla_\mu S_\nu - S^\mu K_{\mu\alpha} + S D_\alpha \ln \alpha = \mathcal{I}_\alpha. \quad (\text{A13})$$

By using

$$\begin{aligned} D_\mu S_\alpha^\mu &:= \gamma_\mu^\rho \gamma_\sigma^\mu \gamma_\alpha^\nu \nabla_\rho S_\nu^\sigma \\ &= \gamma_\alpha^\nu (g_\sigma^\rho + n^\rho n_\sigma) \nabla_\rho S_\nu^\sigma \\ &= \gamma_\alpha^\nu \nabla_\mu S_\nu^\mu + \gamma_\alpha^\nu n^\rho n_\sigma \nabla_\rho S_\nu^\sigma \\ &= \gamma_\alpha^\nu \nabla_\mu S_\nu^\mu - S_\alpha^\mu \nabla_\mu \ln \alpha \end{aligned} \quad (\text{A14})$$

and

$$\begin{aligned} \gamma_\alpha^\nu n^\mu \nabla_\mu S_\nu &= \alpha^{-1} \gamma_\alpha^\nu (\alpha n)^\mu \nabla_\mu S_\nu + \alpha^{-1} \gamma_\alpha^\nu S_\nu \nabla_\mu (\alpha n)^\mu \\ &\quad - \alpha^{-1} \gamma_\alpha^\nu S_\nu \nabla_\mu (\alpha n)^\mu \\ &= \alpha^{-1} \gamma_\alpha^\nu \mathcal{L}_{\alpha n} S_\nu - S_\nu K_\alpha^\nu \\ &= \alpha^{-1} (\partial_t - \mathcal{L}_\beta) S_\alpha - S_\nu K_\alpha^\nu \end{aligned} \quad (\text{A15})$$

we obtain

$$(\partial_t - \mathcal{L}_\beta) S_\alpha + \alpha D_\mu S_\alpha^\mu - \alpha KS_\alpha + S_\alpha^\mu D_\mu \alpha + S D_\alpha \alpha = \alpha \mathcal{I}_\alpha. \quad (\text{A16})$$

To rewrite this into flux divergence form, we expand the Lie-derivative and collect

$$\partial_t S_j + D_i (\alpha S_j^i - \beta^i S_j) + S D_j \alpha - \alpha KS_j + S_j D_i \beta^i - S_i D_j \beta^j = \alpha \mathcal{I}_j. \quad (\text{A17})$$

We can further use that  $D_i (\alpha S_j^i - \beta^i S_j) = \sqrt{\gamma}^{-1} \partial_i [\sqrt{\gamma} (\alpha S_j^i - \beta^i S_j)] - \Gamma_{ji}^k (\alpha S_k^i - \beta^i S_j)$ , and then finally arrive at

$$\begin{aligned} \partial_t (\sqrt{\gamma} S_j) + \partial_i \left[ \sqrt{\gamma} (\alpha S_j^i - \beta^i S_j) \right] = \\ \sqrt{\gamma} \left[ S_i D_j \beta^i - S D_j \alpha + \alpha \mathcal{I}_j + \Gamma_{ji}^k (\alpha S_j^i - \beta^i S_j) \right]. \end{aligned} \quad (\text{A18})$$

This can be further simplified (removing the Christoffel symbol) by noting that

$$D_j \beta^i = \partial_j \beta^i + \Gamma_{jk}^i \beta^k, \quad (\text{A19})$$

and ( $S^{i\ell} = S^{\ell i}$  is symmetric)

$$S_k^i \Gamma_{ji}^k = \frac{1}{2} S_k^i \gamma^{k\ell} (\partial_i \gamma_{\ell j} + \partial_j \gamma_{i\ell} - \partial_\ell \gamma_{ij}), \quad (\text{A20})$$

$$= \frac{1}{2} S^{i\ell} \partial_i \gamma_{\ell j} + \frac{1}{2} S^{i\ell} \partial_j \gamma_{i\ell} - \frac{1}{2} S^{i\ell} \partial_\ell \gamma_{ij}, \quad (\text{A21})$$

$$= \frac{1}{2} S^{i\ell} \partial_j \gamma_{i\ell}. \quad (\text{A22})$$

With the right-hand side simplified we get Eq. 31

$$\begin{aligned} \partial_t (\sqrt{\gamma} S_j) + \partial_i \left[ \sqrt{\gamma} (\alpha S_j^i - \beta^i S_j) \right] \\ = \sqrt{\gamma} \left[ S_i \partial_j \beta^i - S \partial_j \alpha + \frac{1}{2} S^{ik} \partial_j \gamma_{ik} + \alpha \mathcal{I}_j \right]. \end{aligned} \quad (\text{A23})$$

## Appendix B: Primitive recovery scheme of coupled MHD-Proca system

One crucial aspect of any relativistic MHD algorithm is the computation of primitive quantities, such as  $\rho$ ,  $u^\mu$  and  $h$  from the evolved variables. This involves numerical non-linear root finding, which has been well studied in the relativistic case [101, 102, 144–146]. In the following, we extend such a recent scheme [102] to the dark MHD case.

The MHD energy momentum tensor in terms of electric and magnetic field, is [64]

$$\begin{aligned} T_{\text{MHD}}^{\mu\nu} = \rho h u^\mu u^\nu + \frac{1}{2} (E^2 + B^2 + 2p) g^{\mu\nu} \\ - E^\mu E^\nu - B^\mu B^\nu + (n^\mu \varepsilon^{\nu\alpha\beta} + n^\nu \varepsilon^{\mu\alpha\beta}) E_\alpha B_\beta \end{aligned} \quad (\text{B1})$$

The dark current prescription Eq.15, transformed to the normal frame, means the usual ideal MHD prescription  $E^i = -\varepsilon_{ijk} v_j B_k$  is replaced by

$$E^i = -\varepsilon_{ijk} v_j B_k + \bar{\varepsilon} \mu^2 \mathcal{A}^i \Gamma^{-1}, \quad (\text{B2})$$

where  $\bar{\varepsilon} = \varepsilon/\sigma$  and remember the spatial part of Proca field  $\mathcal{A}^\mu = A^\mu + n^\mu n^\nu A'_\nu$ .

The evolved variables (conservatives) are

$$\rho^* = \rho \Gamma, \quad (\text{B3})$$

$$\tau = S - \rho^* = \rho^* (h\Gamma - 1) - p + \frac{E^2 + B^2}{2}, \quad (\text{B4})$$

$$S_i = \rho^* h \Gamma v_i + \varepsilon_{ijk} E^j B^k, \quad (\text{B5})$$

To solve the primitives ( $\rho, p, h, v^i$ ), we follow the idea of [102, 145] by reducing the problem to finding 1D fixed point of a master function.

We first introduce several shorthand notations: the pure fluid contribution of conservatives

$$\tau_{\text{fluid}} = \rho^* (h\Gamma - 1) - p, \quad (\text{B6})$$

$$S_i^{\text{fluid}} = \rho^* h \Gamma v_i, \quad (\text{B7})$$

tilded variables rescaled by  $\rho^*$

$$\tilde{\tau} = \frac{\tau}{\rho^*}, \quad \tilde{\tau}_{\text{fluid}} = \frac{\tau_{\text{fluid}}}{\rho^*}, \quad \tilde{E}_i = \frac{E_i}{\sqrt{\rho^*}}, \quad (\text{B8})$$

$$\tilde{S}_i = \frac{S_i}{\rho^*}, \quad \tilde{S}_i^{\text{fluid}} = \frac{S_i^{\text{fluid}}}{\rho^*}, \quad \tilde{B}_i = \frac{B_i}{\sqrt{\rho^*}}, \quad (\text{B9})$$

shorthand for rescaled Proca field

$$\tilde{a}^i = \frac{\bar{\varepsilon} \mu^2 \mathcal{A}^i}{\rho^*}, \quad (\text{B10})$$

and since  $\bar{\varepsilon}$  here is a small number we ignore terms higher than  $O(\bar{a}^2)$ .

The 1D fixed point strategy we use is introducing a variable  $\mu$ , compute estimators of primitives  $\hat{v}^i, \hat{h}, \dots$  as if  $\mu = 1/(h\Gamma)$  and finally compute the estimator of  $\hat{\mu}$  itself. To get the fixed point of  $\mu$  we find the root of a master function  $f(\mu) = \mu - \hat{\mu}$ . The scheme we introduce below will smoothly reduce to Kastaun's [102] when  $\bar{a} \rightarrow 0$ .

We first note two relations: the relation between the triple products  $[\tilde{S} \tilde{a} \tilde{B}] := \varepsilon_{ijk} \tilde{S}^i \tilde{a}^j \tilde{B}^k$  and  $[\tilde{v} \tilde{a} \tilde{B}] := \varepsilon_{ijk} [\tilde{v}^i \tilde{a}^j \tilde{B}^k]$ :

$$[\tilde{S} \tilde{a} \tilde{B}] = \frac{1 + \mu \tilde{B}^2}{\mu} [\tilde{v} \tilde{a} \tilde{B}] + O(\bar{a}^2), \quad (\text{B11})$$

and the relation between components of  $\tilde{S}^i$  and  $v^i$  parallel to  $\tilde{B}$  (define the parallel component as  $\tilde{S}_\parallel^i := \frac{\tilde{S}^i \tilde{B}_i}{\tilde{B}^2} \tilde{B}^i$ ):

$$\tilde{S}_\parallel^i = \frac{\tilde{B}^j v_j}{\mu \tilde{B}^2} \tilde{B}^i, \quad \text{therefore} \quad \tilde{S}_\parallel^2 = \frac{(\tilde{B}^i v_i)^2}{\mu^2 \tilde{B}^2}. \quad (\text{B12})$$

Then expand the perpendicular component of  $\tilde{S}_i$ ,  $\tilde{S}_\perp^i := \tilde{S}^i - \tilde{S}_\parallel^i$ , and replace the  $\tilde{B}^i v_i$ ,  $[\tilde{v} \tilde{a} \tilde{B}]$  by the two relations above. This gives a quadratic equation for the Lorentz factor  $\Gamma^{-1}$  (note  $v^2 = 1 - \Gamma^{-2}$ , and we use a short hand  $x = \frac{1}{1 + \mu \tilde{B}^2}$ )

$$\tilde{S}_\perp^2 = \frac{1}{x^2 \mu^2} (1 - \Gamma^{-2}) - \frac{\tilde{S}_\parallel^2}{x^2} - [\tilde{S} \tilde{a} \tilde{B}] \Gamma^{-1}, \quad (\text{B13})$$

with discriminant

$$\Delta = 1 - x^2 \mu^2 \tilde{S}_\perp^2 - \mu^2 \tilde{S}_\parallel^2 + \frac{x^4 \mu^4}{4} [\tilde{S} \tilde{a} \tilde{B}]^2. \quad (\text{B14})$$

Our estimator for Lorentz factor is

$$\hat{\Gamma}^{-1} = \sqrt{\hat{\Delta}} - \frac{x^2 \mu^2 [\tilde{S} \tilde{a} \tilde{B}]}{2}, \quad (\text{B15})$$

compared with [102], setting an upper limit for the velocity  $v^2 < v_0^2 := \frac{\tilde{S}^2}{h_0^2 + \tilde{S}^2}$  (with  $h_0$  the lower bound of relativistic enthalpy) is equivalent to setting a lower limit for the discriminant

$$\hat{\Delta} = \max\left\{\Delta, \left(\sqrt{1 - v_0^2} + \frac{x^2 \mu^2 [\tilde{S} \tilde{a} \tilde{B}]}{2}\right)^2\right\}, \quad (\text{B16})$$

which also guarantees the safety of taking square root of  $\hat{\Delta}$  for arbitrary  $\mu$ . Thus the estimator for velocity and fluid momenta will be

$$\hat{v}^2 = 1 - \hat{\Gamma}^{-2}, \quad \tilde{S}_{\text{fluid}}^2 = \frac{\hat{v}^2}{\mu^2}. \quad (\text{B17})$$

The  $1/\mu^2$  in  $\tilde{S}_{\text{fluid}}^2$  may impair numerical safety when  $\mu \rightarrow 0$ , but the  $1/\mu^2$  actually cancel once we expanding everything out, i.e. in code implementation we actually use

$$\tilde{S}_{\text{fluid}}^2 = x^2 \tilde{S}_{\perp}^2 + \tilde{S}_{\parallel}^2 + x^2 [\tilde{S} \tilde{a} \tilde{B}] \sqrt{\hat{\Delta}}, \quad (\text{B18})$$

$$\hat{v}^2 = \min\{\mu^2 \tilde{S}_{\text{fluid}}^2, v_0^2\}, \quad (\text{B19})$$

The equation above may still be negative on rare occasions when the assumed small quantity  $[\tilde{S} \tilde{a} \tilde{B}]$  became large negative numbers compared to  $\tilde{S}_{\perp}^2$ . In that case we floor  $\tilde{S}_{\text{fluid}}^2$  by 0.

Expanding the electric field Eq. B2

$$\begin{aligned} \tilde{E}^2 &= \tilde{B}^2 v^2 - (\tilde{B} \cdot v)^2 + 2\Gamma^{-1} [v \tilde{a} \tilde{B}] + O(\tilde{a}^2), \\ &= \tilde{B}^2 \hat{v}^2 - \mu^2 \tilde{B}^2 \tilde{S}_{\parallel}^2 + 2\hat{\Gamma}^{-1} \frac{\mu [\tilde{S} \tilde{a} \tilde{B}]}{1 + \mu \tilde{B}^2}, \end{aligned} \quad (\text{B20})$$

we also have the estimator for fluid energy

$$\tilde{\tau}_{\text{fluid}} = \tilde{\tau} - \frac{\tilde{E}^2 + \tilde{B}^2}{2}, \quad (\text{B21})$$

Then we have the estimator for the density  $\hat{\rho}$ , internal energy  $\hat{\epsilon}$

$$\hat{\rho} = \rho^* \hat{\Gamma}^{-1}, \quad (\text{B22})$$

$$\hat{\epsilon} = \hat{\Gamma} (\tilde{\tau}_{\text{fluid}} - \mu \tilde{S}_{\text{fluid}}^2) + \frac{\hat{v}^2 \hat{\Gamma}^2}{1 + \hat{\Gamma}}, \quad (\text{B23})$$

and pressure  $\hat{p}$ , specific enthalpy  $\hat{h}$  through equation of state

$$\hat{p} = p(\hat{\rho}, \hat{\epsilon}), \quad (\text{B24})$$

$$\hat{h} = 1 + \hat{\epsilon} + \hat{p}/\hat{\rho}. \quad (\text{B25})$$

Finally we re-express  $\hat{\mu}$  itself by

$$\hat{\mu} = \frac{1}{\hat{h} \hat{\Gamma}^{-1} + \tilde{S}_{\text{fluid}}^2 \mu}. \quad (\text{B26})$$

We see that the scheme defined above smoothly reduces to Kastaun's algorithm [102] when  $\tilde{a} \rightarrow 0$  thus the existence and

uniqueness of solution is guaranteed when Proca field is small enough.

In accordance with Kastaun's algorithm, we make a minor modification to the estimator of  $\nu = \hat{h} \Gamma^{-1}$ , from the estimators above, we have

$$\hat{\nu}_A = (1 + \hat{\epsilon} + \hat{p}/\hat{\rho}) \hat{\Gamma}^{-1}. \quad (\text{B27})$$

Noting another estimator of internal energy

$$\hat{\epsilon}_B = \hat{\Gamma} (\tilde{\tau}_{\text{fluid}} - \mu \tilde{S}_{\text{fluid}}^2) + \hat{\Gamma} - 1, \quad (\text{B28})$$

we can multiply the  $\nu$  estimator by  $\frac{1 + \hat{\epsilon}_B}{1 + \hat{\epsilon}}$  and have

$$\hat{\nu}_B = \left(1 + \frac{\hat{p}}{\hat{\rho}(1 + \hat{\epsilon})}\right) (1 + \tilde{\tau}_{\text{fluid}} - \mu \tilde{S}_{\text{fluid}}^2). \quad (\text{B29})$$

So the actual master function we use is

$$f(\mu) = \mu - \frac{1}{\hat{\nu} + \mu \tilde{S}_{\text{fluid}}^2} \quad (\text{B30})$$

$$\hat{\nu} = \max\{\hat{\nu}_A, \hat{\nu}_B\} \quad (\text{B31})$$

### Appendix C: Accretion disk setup

To set up the accretion disk according to the AJS solution, we first note that the black hole-Proca system can be approximated by a stationary, axisymmetric spacetime

$$ds^2 = g_{tt} dt^2 + 2g_{t\phi} dt d\phi + g_{\phi\phi} d\phi^2 + g_{rr} dr^2 + g_{\theta\theta} d\theta^2, \quad (\text{C1})$$

where the metric components are only dependent on  $(r, \theta)$ . Assuming an ideal fluid circulating around the black hole only in  $\phi$  direction, we have the energy-momentum tensor  $T^{\mu\nu} = \rho h u^\mu u^\nu - p g^{\mu\nu}$  where the fluid velocity  $u^\mu$  only have nonzero  $t$  and  $\phi$  components. Once the specific angular momentum  $l_{\text{AJS}}$  is specified, the fluid velocity distribution is fixed by geodesic equations, with energy

$$\varepsilon_{\text{AJS}} = u_t = -\sqrt{\frac{g_{t\phi}^2 - g_{tt} g_{\phi\phi}}{g_{\phi\phi} + 2l_{\text{AJS}} g_{t\phi} + l_{\text{AJS}}^2 g_{tt}}}, \quad (\text{C2})$$

and angular velocity

$$\omega_{\text{AJS}} = \frac{u^\phi}{u^t} = -\frac{g_{tt} l_{\text{AJS}} + g_{t\phi}}{g_{t\phi} l_{\text{AJS}} + g_{\phi\phi}}. \quad (\text{C3})$$

Then the fluid described by the relativistic Euler equation, as discussed in [128, 147], is governed by the potential  $W_{\text{AJS}}(r, \theta) = \ln \varepsilon_{\text{AJS}}$ . Once the inner edge of the disk, and thereby the maximum potential  $W_{\text{in}}$ , is specified, we set fluid quantities in the places with  $W_{\text{AJS}}(r, \theta) > W_{\text{in}}$  to atmospheric value. Inside the disk  $W_{\text{AJS}}(r, \theta) < W_{\text{in}}$ , we set density  $\rho$ , pressure  $p$  and internal energy  $\varepsilon$  of the fluid according to AJS solution and a simple polytropic equation of state. In the case without Proca field, we tested the analytic solution in Kerr spacetime as discussed in [147]. When the spacetime is modified by Proca field, we set a closed accretion disk with parameter  $l_{\text{AJS}} = 3.22$ ,  $W_{\text{in}} = -0.014141$ , evolved for  $2000M$  time



before we turn on the coupling to the dark sector. The seed magnetic field is initialized as a poloidal field [148]

$$\begin{aligned} A_x &= -y A_b [\max(p - p_{\text{cut}}, 0)]^{n_s}, \\ A_y &= x A_b [\max(p - p_{\text{cut}}, 0)]^{n_s}, \\ A_z &= 0, \end{aligned} \quad (\text{C4})$$

where the pressure  $p$  is the fluid pressure, and we use  $n_s = 2$ ,  $p_{\text{cut}} = 0.04 \max p$  and  $A_b$  such that maximum magnetization  $\bar{\sigma} \approx 50$ . This allows us to fully resolve the magneto-rotational instability (MRI) over a long-time ( $> 6000M$ ) evolution.

- 
- [1] Richard Brito, Vitor Cardoso, and Paolo Pani. Superradiance: New Frontiers in Black Hole Physics. *Lect. Notes Phys.*, 906:pp.1–237, 2015.
- [2] Emanuele Berti et al. Testing General Relativity with Present and Future Astrophysical Observations. *Class. Quant. Grav.*, 32:243001, 2015.
- [3] Nicolás Yunes, Kent Yagi, and Frans Pretorius. Theoretical physics implications of the binary black-hole mergers gw150914 and gw151226. *Phys. Rev. D*, 94:084002, Oct 2016.
- [4] Xi-Long Fan, Kai Liao, Marek Biesiada, Aleksandra Piórkowska-Kurpas, and Zong-Hong Zhu. Speed of gravitational waves from strongly lensed gravitational waves and electromagnetic signals. *Physical review letters*, 118(9):091102, 2017.
- [5] Neil Cornish, Diego Blas, and Germano Nardini. Bounding the speed of gravity with gravitational wave observations. *Physical review letters*, 119(16):161102, 2017.
- [6] Maximiliano Isi, Matthew Pitkin, and Alan J. Weinstein. Probing Dynamical Gravity with the Polarization of Continuous Gravitational Waves. *Phys. Rev. D*, 96(4):042001, 2017.
- [7] Maximiliano Isi, Matthew Giesler, Will M. Farr, Mark A. Scheel, and Saul A. Teukolsky. Testing the no-hair theorem with GW150914. *Phys. Rev. Lett.*, 123(11):111102, 2019.
- [8] Vitor Cardoso and Paolo Pani. Testing the nature of dark compact objects: a status report. *Living Rev. Rel.*, 22(1):4, 2019.
- [9] Karsten Danzmann and the LISA study team. Lisa: laser interferometer space antenna for gravitational wave measurements. *Classical and Quantum Gravity*, 13(11A):A247, 1996.
- [10] RA Konoplya. Shadow of a black hole surrounded by dark matter. *Physics Letters B*, 795:1–6, 2019.
- [11] Samuel E Gralla, Daniel E Holz, and Robert M Wald. Black hole shadows, photon rings, and lensing rings. *Physical Review D*, 100(2):024018, 2019.
- [12] Avery E Broderick, Dominic W Pesce, Roman Gold, Paul Tiede, Hung-Yi Pu, Richard Anantua, Silke Britzen, Chiara Ceccobello, Koushik Chatterjee, Yongjun Chen, et al. The photon ring in m87. *The Astrophysical Journal*, 935(1):61, 2022.
- [13] Michael Kramer, Ingrid H Stairs, RN Manchester, MA McLaughlin, AG Lyne, RD Ferdman, M Burgay, DR Lorimer, A Possenti, Nicolo’ D’Amico, et al. Tests of general relativity from timing the double pulsar. *science*, 314(5796):97–102, 2006.
- [14] Nicolás Yunes and Xavier Siemens. Gravitational-wave tests of general relativity with ground-based detectors and pulsar-timing arrays. *Living Reviews in Relativity*, 16(1):1–124, 2013.
- [15] Neil J. Cornish, Logan O’Beirne, Stephen R. Taylor, and Nicolás Yunes. Constraining alternative theories of gravity using pulsar timing arrays. *Phys. Rev. Lett.*, 120(18):181101, 2018.
- [16] Emanuele Berti, Vitor Cardoso, Zoltán Haiman, Daniel E. Holz, Emil Mottola, Suvodip Mukherjee, Bangalore Sathyaprakash, Xavier Siemens, and Nicolás Yunes. Snowmass2021 Cosmic Frontier White Paper: Fundamental Physics and Beyond the Standard Model. In *Snowmass 2021*, 3 2022.
- [17] Masha Baryakhtar et al. Dark Matter In Extreme Astrophysical Environments. In *Snowmass 2021*, 3 2022.
- [18] Daniel Baumann, Horng Sheng Chia, and Rafael A Porto. Probing ultralight bosons with binary black holes. *Physical Review D*, 99(4):044001, 2019.
- [19] Maximiliano Isi, Ling Sun, Richard Brito, and Andrew Melatos. Directed searches for gravitational waves from ultralight bosons. *Physical Review D*, 99(8):084042, 2019.
- [20] Juan Calderón Bustillo, Nicolas Sanchis-Gual, Alejandro Torres-Forné, José A Font, Avi Vajpeyi, Rory Smith, Carlos Herdeiro, Eugen Radu, and Samson HW Leong. Gw190521 as a merger of proca stars: a potential new vector boson of  $8.7 \times 10^{-13}$  eV. *Physical Review Letters*, 126(8):081101, 2021.
- [21] Peter Svrcek and Edward Witten. Axions in string theory. *Journal of High Energy Physics*, 2006(06):051, 2006.
- [22] Asimina Arvanitaki, Savvas Dimopoulos, Sergei Dubovsky, Nemanja Kaloper, and John March-Russell. String axiverse. *Physical Review D*, 81(12):123530, 2010.
- [23] Adi Nusser, Steven S Gubser, and PJE Peebles. Structure formation with a long-range scalar dark matter interaction. *Physical Review D*, 71(8):083505, 2005.
- [24] Pau Amaro-Seoane et al. eLISA/NGO: Astrophysics and cosmology in the gravitational-wave millihertz regime. *GW Notes*, 6:4–110, 2013.
- [25] Pau Amaro Seoane et al. The Gravitational Universe. 5 2013.
- [26] Steven Weinberg. A new light boson? *Physical Review Letters*, 40(4):223, 1978.
- [27] Lev Borisovich Okun. Limits of electrodynamics: paraphotons. Technical report, Gosudarstvennyj Komitet po Ispol’zovaniyu Atomnoj Ehnergii SSSR, 1982.
- [28] Jonathan L Feng, Manoj Kaplinghat, Huitzu Tu, and Hai-Bo Yu. Hidden charged dark matter. *Journal of Cosmology and Astroparticle Physics*, 2009(07):004, 2009.
- [29] Francis-Yan Cyr-Racine and Kris Sigurdson. Cosmology of atomic dark matter. *Physical Review D*, 87(10):103515, 2013.
- [30] Amit Bhoonah, Joseph Bramante, Fatemeh Elahi, and Sarah Schon. Galactic center gas clouds and novel bounds on ultralight dark photon, vector portal, strongly interacting, composite, and super-heavy dark matter. *Physical Review D*, 100(2):023001, 2019.
- [31] Jacob D. Bekenstein. Extraction of energy and charge from a black hole. *Phys. Rev. D*, 7:949–953, Feb 1973.
- [32] João G. Rosa and Sam R. Dolan. Massive vector fields on the schwarzschild spacetime: Quasinormal modes and bound states. *Phys. Rev. D*, 85:044043, Feb 2012.
- [33] Brito Richard, Cardoso Vitor, and Pani Paolo. Superradiance: New frontiers in black hole physics. *Lect. Notes Phys.*, 906:1–237, 2015.
- [34] Asimina Arvanitaki, Masha Baryakhtar, and Xinlu Huang. Discovering the qcd axion with black holes and gravitational



- waves. *Physical Review D*, 91(8):084011, 2015.
- [35] Asimina Arvanitaki, Masha Baryakhtar, Savas Dimopoulos, Sergei Dubovsky, and Robert Lasenby. Black hole mergers and the qcd axion at advanced ligo. *Physical Review D*, 95(4):043001, 2017.
- [36] Valeri P Frolov, Pavel Krtouš, David Kubizňák, and Jorge E Santos. Massive vector fields in rotating black-hole spacetimes: separability and quasinormal modes. *Physical Review Letters*, 120(23):231103, 2018.
- [37] Sam R Dolan. Instability of the proca field on kerr spacetime. *Physical Review D*, 98(10):104006, 2018.
- [38] Nils Siemonsen and William E East. Gravitational wave signatures of ultralight vector bosons from black hole superradiance. *Physical Review D*, 101(2):024019, 2020.
- [39] Helvi Wittek, Vitor Cardoso, Akihiro Ishibashi, and Ulrich Sperhake. Superradiant instabilities in astrophysical systems. *Physical Review D*, 87(4):043513, 2013.
- [40] Miguel Zilhão, Helvi Wittek, and Vitor Cardoso. Nonlinear interactions between black holes and proca fields. *Classical and Quantum Gravity*, 32(23):234003, 2015.
- [41] William E East. Superradiant instability of massive vector fields around spinning black holes in the relativistic regime. *Physical Review D*, 96(2):024004, 2017.
- [42] William E East and Frans Pretorius. Superradiant instability and backreaction of massive vector fields around kerr black holes. *Physical review letters*, 119(4):041101, 2017.
- [43] Zipeng Wang, Thomas Helfer, Katy Clough, and Emanuele Berti. Superradiance in massive vector fields with spatially varying mass. *Physical Review D*, 105(10):104055, 2022.
- [44] RA Konoplya. Massive vector field perturbations in the schwarzschild background: Stability and quasinormal spectrum. *Physical Review D*, 73(2):024009, 2006.
- [45] RA Konoplya, Alexander Zhidenko, and Carlos Molina. Late time tails of the massive vector field in a black hole background. *Physical Review D*, 75(8):084004, 2007.
- [46] Helvi Wittek, David Hilditch, and Ulrich Sperhake. Stability of the puncture method with a generalized baumgarte-shapiro-shibata-nakamura formulation. *Physical Review D*, 83(10):104041, 2011.
- [47] Joao G Rosa and Sam R Dolan. Massive vector fields on the schwarzschild spacetime: quasinormal modes and bound states. *Physical Review D*, 85(4):044043, 2012.
- [48] Paolo Pani, Vitor Cardoso, Leonardo Gualtieri, Emanuele Berti, and Akihiro Ishibashi. Black-hole bombs and photon-mass bounds. *Physical review letters*, 109(13):131102, 2012.
- [49] Paolo Pani, Vitor Cardoso, Leonardo Gualtieri, Emanuele Berti, and Akihiro Ishibashi. Perturbations of slowly rotating black holes: massive vector fields in the kerr metric. *Physical Review D*, 86(10):104017, 2012.
- [50] Masha Baryakhtar, Robert Lasenby, and Mae Teo. Black hole superradiance signatures of ultralight vectors. *Physical Review D*, 96(3):035019, 2017.
- [51] Solomon Endlich and Riccardo Penco. A modern approach to superradiance. *Journal of High Energy Physics*, 2017(5):1–39, 2017.
- [52] Richard Brito, Shrobona Ghosh, Enrico Barausse, Emanuele Berti, Vitor Cardoso, Irina Dvorkin, Antoine Klein, and Paolo Pani. Gravitational wave searches for ultralight bosons with ligo and lisa. *Physical Review D*, 96(6):064050, 2017.
- [53] Leo Tsukada, Richard Brito, William E. East, and Nils Siemonsen. Modeling and searching for a stochastic gravitational-wave background from ultralight vector bosons. *Phys. Rev. D*, 103(8):083005, 2021.
- [54] Vicky Kalogera et al. The Next Generation Global Gravitational Wave Observatory: The Science Book. 11 2021.
- [55] Dana Jones, Ling Sun, Nils Siemonsen, William E East, Susan M Scott, and Karl Wette. Methods and prospects for gravitational-wave searches targeting ultralight vector-boson clouds around known black holes. *Physical Review D*, 108(6):064001, 2023.
- [56] Roger D Blandford and Roman L Znajek. Electromagnetic extraction of energy from kerr black holes. *Monthly Notices of the Royal Astronomical Society*, 179(3):433–456, 1977.
- [57] Leslie G Fishbone and Vincent Moncrief. Relativistic fluid disks in orbit around kerr black holes. *The Astrophysical Journal*, 207:962–976, 1976.
- [58] Hyun Kyu Lee, Ralph Antoine Marie Joseph Wijers, and Gerald Edward Brown. The blandford–znajek process as a central engine for a gamma-ray burst. *Physics Reports*, 325(3):83–114, 2000.
- [59] Roger Blandford, David Meier, and Anthony Readhead. Relativistic jets from active galactic nuclei. *Annual Review of Astronomy and Astrophysics*, 57:467–509, 2019.
- [60] Nils Siemonsen, Cristina Mondino, Daniel Egaña-Ugrinovic, Junwu Huang, Masha Baryakhtar, and William E East. Dark photon superradiance: Electrodynamics and multimessenger signals. *Physical Review D*, 107(7):075025, 2023.
- [61] Yosuke Mizuno, Ziri Younsi, Christian M. Fromm, Oliver Porth, Mariafelicia De Laurentis, Hector Olivares, Heino Falcke, Michael Kramer, and Luciano Rezzolla. The Current Ability to Test Theories of Gravity with Black Hole Shadows. *Nature Astron.*, 2(7):585–590, 2018.
- [62] Hector Olivares, Ziri Younsi, Christian M Fromm, Mariafelicia De Laurentis, Oliver Porth, Yosuke Mizuno, Heino Falcke, Michael Kramer, and Luciano Rezzolla. How to tell an accreting boson star from a black hole. *Monthly Notices of the Royal Astronomical Society*, 497(1):521–535, 2020.
- [63] Yifan Chen, Yuxin Liu, Ru-Sen Lu, Yosuke Mizuno, Jing Shu, Xiao Xue, Qiang Yuan, and Yue Zhao. Stringent axion constraints with Event Horizon Telescope polarimetric measurements of M87. *Nature Astron.*, 6(5):592–598, 2022.
- [64] Thomas W Baumgarte and Stuart L Shapiro. General relativistic magnetohydrodynamics for the numerical construction of dynamical spacetimes. *The Astrophysical Journal*, 585(2):921, 2003.
- [65] Saul A Teukolsky. Perturbations of a rotating black hole. 1. fundamental equations for gravitational electromagnetic and neutrino field perturbations. *Astrophys. J.*, 185:635–647, 1973.
- [66] William H Press and Saul A Teukolsky. Perturbations of a rotating black hole. ii. dynamical stability of the kerr metric. *The Astrophysical Journal*, 185:649–674, 1973.
- [67] Saul A Teukolsky and WH Press. Perturbations of a rotating black hole. iii-interaction of the hole with gravitational and electromagnetic radiation. *The Astrophysical Journal*, 193:443–461, 1974.
- [68] Misao Sasaki and Takashi Nakamura. Gravitational Radiation From a Kerr Black Hole. 1. Formulation and a Method for Numerical Analysis. *Prog. Theor. Phys.*, 67:1788, 1982.
- [69] Scott A. Hughes. Computing radiation from Kerr black holes: Generalization of the Sasaki-Nakamura equation. *Phys. Rev. D*, 62:044029, 2000. [Erratum: Phys.Rev.D 67, 089902 (2003)].
- [70] Misao Sasaki and Hideyuki Tagoshi. Analytic black hole perturbation approach to gravitational radiation. *Living Reviews in Relativity*, 6(1):6, Nov 2003.

- [71] Rico K. L. Lo. Recipes for computing radiation from a Kerr black hole using Generalized Sasaki-Nakamura formalism: I. Homogeneous solutions. 6 2023.
- [72] Elisa Maggio, Vitor Cardoso, Sam R. Dolan, and Paolo Pani. Ergoregion instability of exotic compact objects: Electromagnetic and gravitational perturbations and the role of absorption. *Phys. Rev. D*, 99:064007, Mar 2019.
- [73] Rodrigo Vicente, Vitor Cardoso, and Jorge C. Lopes. Penrose process, superradiance, and ergoregion instabilities. *Phys. Rev. D*, 97:084032, Apr 2018.
- [74] Mauricio Richartz, Silke Weinfurter, A. J. Penner, and W. G. Unruh. Generalized superradiant scattering. *Phys. Rev. D*, 80:124016, Dec 2009.
- [75] Vitor Cardoso and Paolo Pani. Tests for the existence of black holes through gravitational wave echoes. *Nature Astronomy*, 1(9):586, 2017.
- [76] Shuo Xin, Baoyi Chen, Rico K. L. Lo, Ling Sun, Wen-Biao Han, Xingyu Zhong, Manu Srivastava, Sizheng Ma, Qingwen Wang, and Yanbei Chen. Gravitational-wave echoes from spinning exotic compact objects: Numerical waveforms from the Teukolsky equation. *Phys. Rev. D*, 104(10):104005, 2021.
- [77] Elisa Maggio, Maarten van de Meent, and Paolo Pani. Extreme mass-ratio inspirals around a spinning horizonless compact object. *Phys. Rev. D*, 104(10):104026, 2021.
- [78] Randy S. Conklin and Niayesh Afshordi. Boltzmann Meets Lorentz: A Surrogate Model for Black Hole Echoes. 12 2021.
- [79] Sizheng Ma, Qingwen Wang, Nils Deppe, François Hébert, Lawrence E. Kidder, Jordan Moxon, William Throwe, Nils L. Vu, Mark A. Scheel, and Yanbei Chen. Gravitational-wave echoes from numerical-relativity waveforms via spacetime construction near merging compact objects. *Phys. Rev. D*, 105(10):104007, 2022.
- [80] Masha Baryakhtar, Regina Caputo, Djuna Croon, Kerstin Perez, Emanuele Berti, Joseph Bramante, Malte Buschmann, Richard Brito, Thomas Y Chen, Philippa S Cole, et al. Dark matter in extreme astrophysical environments. *arXiv preprint arXiv:2203.07984*, 2022.
- [81] William H Press and Saul A Teukolsky. Floating orbits, superradiant scattering and the black-hole bomb. *Nature*, 238(5361):211–212, 1972.
- [82] Helvi Witek, Vitor Cardoso, Akihiro Ishibashi, and Ulrich Sperhake. Superradiant instabilities in astrophysical systems. *Phys. Rev. D*, 87:043513, Feb 2013.
- [83] Ethan Payne, Ling Sun, Kyle Kremer, Paul D Lasky, and Eric Thrane. The imprint of superradiance on hierarchical black hole mergers. *The Astrophysical Journal*, 931(2):79, 2022.
- [84] Hiroko Koyama and Akira Tomimatsu. Slowly decaying tails of massive scalar fields in spherically symmetric spacetimes. *Physical Review D*, 65(8):084031, 2002.
- [85] Kazunori Akiyama, Juan Carlos Algaba, Antxon Alberdi, Walter Alef, Richard Anantua, Keiichi Asada, Rebecca Azuly, Anne-Kathrin Baczko, David Ball, Mislav Baloković, et al. First m87 event horizon telescope results. viii. magnetic field structure near the event horizon. *The Astrophysical Journal Letters*, 910(1):L13, 2021.
- [86] Christopher S Reynolds. Observational constraints on black hole spin. *Annual Review of Astronomy and Astrophysics*, 59:117–154, 2021.
- [87] Mitchell C Begelman, Roger D Blandford, and Martin J Rees. Theory of extragalactic radio sources. *Reviews of Modern Physics*, 56(2):255, 1984.
- [88] Roger D Blandford and DG Payne. Hydromagnetic flows from accretion discs and the production of radio jets. *Monthly Notices of the Royal Astronomical Society*, 199(4):883–903, 1982.
- [89] Ramesh Narayan and Insu Yi. Advection-dominated accretion: Underfed black holes and neutron stars. *arXiv preprint astro-ph/9411059*, 1994.
- [90] Ramesh Narayan, Rohan Mahadevan, Jonathan E Grindlay, Robert G Popham, and Charles Gammie. Advection-dominated accretion model of sagittarius a\*: evidence for a black hole at the galactic center. *The Astrophysical Journal*, 492(2):554, 1998.
- [91] Feng Yuan, Sera Markoff, and Heino Falcke. A jet-adaf model for sgr a. *Astronomy & Astrophysics*, 383(3):854–863, 2002.
- [92] Elias R Most and Alexander A Philippov. Electromagnetic precursor flares from the late inspiral of neutron star binaries. *Monthly Notices of the Royal Astronomical Society*, 515(2):2710–2724, 2022.
- [93] We use  $\epsilon$  for the kinetic dark matter coupling and  $\varepsilon$  for the Levi-Civita tensor.
- [94] Elias R Most. Impact of a mean field dynamo on neutron star mergers leading to magnetar remnants. *Physical Review D*, 108(12):123012, 2023.
- [95] Elias R. Most, Jorge Noronha, and Alexander A. Philippov. Modelling general-relativistic plasmas with collisionless moments and dissipative two-fluid magnetohydrodynamics. *Mon. Not. Roy. Astron. Soc.*, 514(4):4989–5003, 2022.
- [96] Masaru Shibata and Yu-ichirou Sekiguchi. Magnetohydrodynamics in full general relativity: Formulation and tests. *Physical Review D*, 72(4):044014, 2005.
- [97] Ericourgoulhon. 3+ 1 formalism and bases of numerical relativity. *arXiv preprint gr-qc/0703035*, 2007.
- [98] Masaru Shibata and Takashi Nakamura. Evolution of three-dimensional gravitational waves: Harmonic slicing case. *Phys. Rev. D*, 52:5428–5444, Nov 1995.
- [99] Thomas W. Baumgarte and Stuart L. Shapiro. Numerical integration of einstein’s field equations. *Phys. Rev. D*, 59:024007, Dec 1998.
- [100] Zachariah B Etienne, Vasileios Paschalidis, Yuk Tung Liu, and Stuart L Shapiro. Relativistic mhd in dynamical spacetimes: Improved em gauge condition for amr grids. *arXiv preprint arXiv:1110.4633*, 2011.
- [101] Scott C. Noble, Charles F. Gammie, Jonathan C. McKinney, and Luca Del Zanna. Primitive variable solvers for conservative general relativistic magnetohydrodynamics. *Astrophys. J.*, 641:626–637, 2006.
- [102] Wolfgang Kastaun, Jay Vijay Kalinani, and Riccardo Ciolfi. Robust recovery of primitive variables in relativistic ideal magnetohydrodynamics. *Physical Review D*, 103(2):023018, 2021.
- [103] Frank Löffler, Joshua Faber, Eloisa Bentivegna, Tanja Bode, Peter Diener, Roland Haas, Ian Hinder, Bruno C Mundim, Christian D Ott, Erik Schnetter, et al. The einstein toolkit: a community computational infrastructure for relativistic astrophysics. *Classical and Quantum Gravity*, 29(11):115001, 2012.
- [104] Helvi Witek, Miguel Zilhao, Giuseppe Ficarra, and Matthew Elley. Canuda: a public numerical relativity library to probe fundamental physics, 2021.
- [105] Carlos AR Herdeiro, Alexandre M Pombo, Eugen Radu, Pedro VP Cunha, and Nicolas Sanchis-Gual. The imitation game: Proca stars that can mimic the schwarzschild shadow. *Journal of Cosmology and Astroparticle Physics*, 2021(04):051, 2021.
- [106] Elias R. Most, L. Jens Papenfort, and Luciano Rezzolla. Beyond second-order convergence in simulations of magnetized binary neutron stars with realistic microphysics. *Mon. Not.*

- Roy. Astron. Soc.*, 490(3):3588–3600, 2019.
- [107] Zachariah B. Etienne, Vasileios Paschalidis, Roland Haas, Philipp Mösta, and Stuart L. Shapiro. IllinoisGRMHD: An Open-Source, User-Friendly GRMHD Code for Dynamical Spacetimes. *Class. Quant. Grav.*, 32:175009, 2015.
- [108] Zachariah B. Etienne, Vasileios Paschalidis, Yuk Tung Liu, and Stuart L. Shapiro. Relativistic magnetohydrodynamics in dynamical spacetimes: Improved electromagnetic gauge condition for adaptive mesh refinement grids. *Phys. Rev. D*, 85:024013, Jan 2012.
- [109] Luca Del Zanna, Olindo Zanotti, N Bucciantini, and P Londrillo. Echo: a eulerian conservative high-order scheme for general relativistic magnetohydrodynamics and magnetodynamics. *Astronomy & Astrophysics*, 473(1):11–30, 2007.
- [110] Elias R. Most, L. Jens Papenfort, Samuel D. Tootle, and Luciano Rezzolla. On accretion discs formed in MHD simulations of black hole–neutron star mergers with accurate microphysics. *Mon. Not. Roy. Astron. Soc.*, 506(3):3511–3526, 2021.
- [111] Michail Chabanov, Samuel D. Tootle, Elias R. Most, and Luciano Rezzolla. Crustal Magnetic Fields Do Not Lead to Large Magnetic-field Amplifications in Binary Neutron Star Mergers. *Astrophys. J. Lett.*, 945(1):L14, 2023.
- [112] Elias R. Most and Eliot Quataert. Flares, Jets, and Quasiperiodic Outbursts from Neutron Star Merger Remnants. *Astrophys. J. Lett.*, 947(1):L15, 2023.
- [113] Elias R. Most. Impact of a mean field dynamo on neutron star mergers leading to magnetar remnants. *Phys. Rev. D*, 108(12):123012, 2023.
- [114] Elias R. Most, Andrei M. Beloborodov, and Bart Ripperda. Monster shocks, gamma-ray bursts and black hole quasinormal modes from neutron-star collapse. 4 2024.
- [115] Sebastiano Bernuzzi and David Hilditch. Constraint violation in free evolution schemes: Comparing BSSNOK with a conformal decomposition of Z4. *Phys. Rev. D*, 81:084003, 2010.
- [116] David Hilditch, Sebastiano Bernuzzi, Marcus Thierfelder, Zhoujian Cao, Wolfgang Tichy, and Bernd Bruegmann. Compact binary evolutions with the Z4c formulation. *Phys. Rev. D*, 88:084057, 2013.
- [117] Miguel Alcubierre, Bernd Brügmann, Peter Diener, F Siddhartha Guzmán, Ian Hawke, Scott Hawley, Frank Herrmann, Michael Koppitz, Denis Pollney, Edward Seidel, et al. Dynamical evolution of quasicircular binary black hole data. *Physical Review D*, 72(4):044004, 2005.
- [118] Yosef Zlochower, John G Baker, Manuela Campanelli, and Carlos O Lousto. Accurate black hole evolutions by fourth-order numerical relativity. *Physical Review D*, 72(2):024021, 2005.
- [119] Frank Löffler, Joshua Faber, Eloisa Bentivegna, Tanja Bode, Peter Diener, Roland Haas, Ian Hinder, Bruno C Mundim, Christian D Ott, Erik Schnetter, et al. The einstein toolkit: a community computational infrastructure for relativistic astrophysics. *Classical and Quantum Gravity*, 29(11):115001, 2012.
- [120] Erik Schnetter, Scott H. Hawley, and Ian Hawke. Evolutions in 3-D numerical relativity using fixed mesh refinement. *Class. Quant. Grav.*, 21:1465–1488, 2004.
- [121] Steven Brandt and Bernd Brügmann. A simple construction of initial data for multiple black holes. *Physical Review Letters*, 78(19):3606, 1997.
- [122] Helvi Witek, Miguel Zilhao, Giuseppe Ficarra, and Matthew Elley. Canuda: a public numerical relativity library to probe fundamental physics, May 2020.
- [123] Ramesh Narayan and In-su Yi. Advection dominated accretion: A Selfsimilar solution. *Astrophys. J. Lett.*, 428:L13, 1994.
- [124] Ramesh Narayan and Jeffrey E. McClintock. Advection-Dominated Accretion and the Black Hole Event Horizon. *New Astron. Rev.*, 51:733–751, 2008.
- [125] Kyle Parfrey, Alexander Philippov, and Benoît Cerutti. First-Principles Plasma Simulations of Black-Hole Jet Launching. *Phys. Rev. Lett.*, 122(3):035101, 2019.
- [126] Serguei S. Komissarov. Electrically charged black holes and the Blandford–Znajek mechanism. *Mon. Not. Roy. Astron. Soc.*, 512(2):2798–2805, 2022.
- [127] Shane W. Davis and Alexander Tchekhovskoy. Magnetohydrodynamics Simulations of Active Galactic Nucleus Disks and Jets. *Ann. Rev. Astron. Astrophys.*, 58:407–439, 2020.
- [128] M Abramowicz, M Jaroszynski, and M Sikora. Relativistic, accreting disks. *Astronomy and Astrophysics*, vol. 63, no. 1-2, Feb. 1978, p. 221-224., 63:221–224, 1978.
- [129] Alexander Tchekhovskoy, Ramesh Narayan, and Jonathan C McKinney. Efficient generation of jets from magnetically arrested accretion on a rapidly spinning black hole. *Monthly Notices of the Royal Astronomical Society: Letters*, 418(1):L79–L83, 2011.
- [130] Bart Ripperda, Matthew Liska, Koushik Chatterjee, Gibwa Musoke, Alexander A. Philippov, Sera B. Markoff, Alexander Tchekhovskoy, and Ziri Younsi. Black Hole Flares: Ejection of Accreted Magnetic Flux through 3D Plasmoid-mediated Reconnection. *Astrophys. J. Lett.*, 924(2):L32, 2022.
- [131] N. Bucciantini and L. Del Zanna. A fully covariant mean-field dynamo closure for numerical 3+1 resistive GRMHD. *Mon. Not. Roy. Astron. Soc.*, 428:71, 2013.
- [132] Zhaohuan Zhu and James M. Stone. Global evolution of an accretion disk with a net vertical field: Coronal accretion, flux transport, and disk winds. *The Astrophysical Journal*, 857(1):34, apr 2018.
- [133] L. Mestel. A Note on Equatorial Acceleration in a Magnetic Star. *Monthly Notices of the Royal Astronomical Society*, 122(6):473–478, 06 1961.
- [134] L. Mestel. Magnetic Braking by a Stellar Wind—I. *Monthly Notices of the Royal Astronomical Society*, 138(3):359–391, 02 1968.
- [135] Jeffrey M. Anderson, Zhi-Yun Li, Ruben Krasnopolsky, and Roger D. Blandford. The structure of magnetocentrifugal winds. i. steady mass loading. *The Astrophysical Journal*, 630(2):945, sep 2005.
- [136] Helvi Witek, Miguel Zilhao, Gabriele Bozzola, Matthew Elley, Giuseppe Ficarra, Taishi Ikeda, Nicolas Sanchis-Gual, and Hector Silva. Canuda: a public numerical relativity library to probe fundamental physics, October 2021.
- [137] Kazunori Akiyama et al. First M87 Event Horizon Telescope Results. V. Physical Origin of the Asymmetric Ring. *Astrophys. J. Lett.*, 875(1):L5, 2019.
- [138] Event Horizon Telescope Collaborat. First m87 event horizon telescope results. i. the shadow of the supermassive black hole. *Astrophysical Journal Letters*, 875(1):L1, 2019.
- [139] Oliver Porth, Koushik Chatterjee, Ramesh Narayan, Charles F Gammie, Yosuke Mizuno, Peter Anninos, John G Baker, Matteo Bugli, Chi-kwan Chan, Jordy Davelaar, et al. The event horizon general relativistic magnetohydrodynamic code comparison project. *The Astrophysical Journal Supplement Series*, 243(2):26, 2019.
- [140] Jiaru Li, Adam M. Dempsey, Hui Li, Dong Lai, and Shengtai Li. Hydrodynamical Simulations of Black Hole Binary Formation in AGN Disks. *Astrophys. J. Lett.*, 944(2):L42, Febru-

- ary 2023.
- [141] Alexander J. Dittmann, Adam M. Dempsey, and Hui Li. The Evolution of Inclined Binary Black Holes in the Disks of Active Galactic Nuclei. *Astrophys. J.*, 964(1):61, 2024.
- [142] Diogo C Ribeiro, Miguel Zilhão, and Vitor Cardoso. Binary superradiance: A numerical study. *Physical Review D*, 105(8):084004, 2022.
- [143] Jamie Bamber, Josu C. Aurrekoetxea, Katy Clough, and Pedro G. Ferreira. Black hole merger simulations in wave dark matter environments. *Phys. Rev. D*, 107(2):024035, 2023.
- [144] Carlos Palenzuela, Steven L Liebling, David Neilsen, Luis Lehner, OL Caballero, Evan O'Connor, and Matthew Anderson. Effects of the microphysical equation of state in the mergers of magnetized neutron stars with neutrino cooling. *Physical Review D*, 92(4):044045, 2015.
- [145] Bart Ripperda, Fabio Bacchini, Oliver Porth, Elias R Most, Hector Olivares, Antonios Nathanail, Luciano Rezzolla, Janis Teunissen, and Rony Keppens. General-relativistic resistive magnetohydrodynamics with robust primitive-variable recovery for accretion disk simulations. *The Astrophysical Journal Supplement Series*, 244(1):10, 2019.
- [146] Harry Ho-Yin Ng, Jin-Liang Jiang, Carlo Musolino, Christian Ecker, Samuel D Tootle, and Luciano Rezzolla. A hybrid approach to long-term binary neutron-star simulations. *arXiv preprint arXiv:2312.11358*, 2023.
- [147] M Kozłowski, M Jaroszynski, and MA Abramowicz. The analytic theory of fluid disks orbiting the kerr black hole. *Astronomy and Astrophysics*, vol. 63, no. 1-2, Feb. 1978, p. 209-220. *Research supported by the Universita di Padova.*, 63:209–220, 1978.
- [148] Zachariah B. Etienne, Vasileios Paschalidis, Roland Haas, Philipp Mösta, and Stuart L. Shapiro. IllinoisGRMHD: an open-source, user-friendly GRMHD code for dynamical spacetimes. *Classical and Quantum Gravity*, 32(17):175009, September 2015.